A Close Look at Star Formation around Active Galactic Nuclei[1]

R. I. Davies, F. Mueller Sánchez, R. Genzel, L.J. Tacconi, E.K.S. Hicks, S. Friedrich,

Max Planck Institut für extraterrestrische Physik, Postfach 1312, 85741, Garching, Germany

and

A. Sternberg

School of Physics and Astronomy, Tel Aviv University, Tel Aviv 69978, Israel

ABSTRACT

We analyse star formation in the nuclei of 9 Seyfert galaxies at spatial resolutions down to $0.085''$, corresponding to length scales of order $10\,\mathrm{pc}$ in most objects. Our data were taken mostly with the near infrared adaptive optics integral field spectrograph SINFONI. The stellar light profiles typically have size scales of a few tens of parsecs. In two cases there is unambiguous kinematic evidence for stellar disks on these scales. In the nuclear regions there appear to have been recent – but no longer active – starbursts in the last 10-300 Myr. The stellar luminosity is less than a few percent of the AGN in the central $10\,\mathrm{pc}$, whereas on kiloparsec scales the luminosities are comparable. The surface stellar luminosity density follows a similar trend in all the objects, increasing steadily at smaller radii up to $\sim 10^{13}\,\mathrm{L_\odot\,kpc^{-2}}$ in the central few parsecs, where the mass surface density exceeds $10^4\,\mathrm{M_\odot\,pc^{-2}}$. The intense starbursts were probably Eddington limited and hence inevitably short-lived, implying that the starbursts occur in multiple short bursts. The data hint at a delay of 50–100 Myr between the onset of star formation and subsequent fuelling of the black hole. We discuss whether this may be a consequence of the role that stellar ejecta could play in fuelling the black hole. While a significant mass is ejected by OB winds and supernovae, their high velocity means that very little of it can be accreted. On the other hand winds from AGB stars ultimately dominate the total mass loss, and they can also be accreted very efficiently because of their slow speeds.

Subject headings: galaxies: active — galaxies: nuclei — galaxies: Seyfert — galaxies: starburst — infrared: galaxies

1. Introduction

During recent years there has been increasing evidence for a connection between active galactic nuclei (AGN) and star formation in the vicinity of the central black holes. This subject forms the central topic of this paper, and is discussed in Sections 4 and 5.

A large number of studies have addressed the issue of star formation around AGN. Those which have probed closest to the nucleus, typically on scales of a few hundred parsecs, have tended to focus on Seyferts – notably Seyfert 2 galaxies – since these are the closest examples (Sarzi et al. 2007; Asari et el. 2007;

González Delgado, et al. 2005; Cid Fernandes et al. 2004; González Delgado, et al. 2001; Gu et al. 2001; Joguet et al. 2001; Storchi-Bergmann et al. 2001; Ivanov et al. 2000). The overall conclusion of these studies is that in 30–50% cases the AGN is associated with young (i.e. age less than a few 100 Myr) star formation. While this certainly implies a link, it does not necessarily imply any *causal* link between the two phenomena. Instead, it could more simply be a natural consequence of the fact that both AGN and starburst require gas to fuel them. And that in some galaxies this gas has fallen towards the nucleus, either due to an interaction or secular evolution such as bar driven inflow.

One aspect which must be borne in mind when interpreting such results, and which has been pointed out by Knapen (2004), is the discrepancy in the scales involved. AGN and starburst phemonena occur on different temporal and spatial scales; and observations are sensitive to scales that are different again. For example, star formation has typically been studied on scales of several kiloparsecs down to a few hundred parsecs. In contrast, accretion of gas onto an AGN will occur on scales much less than 1 pc. Similarly, the shortest star formation timescales that most observations are sensitive to are of order 100 Myr to 1 Gyr. On the other hand, in this paper we show that the active phase of star formation close around a black hole is typically rather less than 100 Myr. Correspondingly short accretion timescales for black holes are reflected in the ages of jets which, for a sample of radio galaxies measured by Machalski et al. (2007), span a range from a few to 100 Myr. In Seyfert galaxies the timescales are even shorter, as typified by NGC 1068 for which Capetti et al. (1999) estimate the age of the jets to be only ~ 0.1 Myr. That the putative causal connection between AGN and starbursts might occur on relatively small spatial scales and short timescales can help us to understand why no correlation has been found between AGN and (circum-)nuclear starbursts in general. It is simply that the circumnuclear activity on scales greater than a few hundred parsecs is, in most cases, too far from the AGN to influence it, or be strongly influenced by it (cf Heckman et al. 1997).

In this paper we redress this imbalance. While the optical spectroscopy pursued by many authors allows a detailed fitting of templates and models to the stellar features, we also make use of established star formation diagnostics and interpret them using starburst population synthesis models. Observing at near infrared wavelengths has brought two important advantages. The optical depth is 10 times less than at optical wavelengths, and thus our data are less prone to the effects of extinction which can be significant in AGN. And we have employed adaptive optics to reach spatial resolutions of 0.1–$0.2''$, bringing us closer to the nucleus. Applying these techniques, we have already analysed the properties of the nuclear star formation in a few objects (Davies et al. 2004a,b, 2006; Mueller Sánchez et al. 2006). Here we bring those data together with new data on 5 additional objects. Our sample enables us to probe star formation in AGN from radii of 1 kpc down to less than 10 pc. Our aim is to ascertain whether there is evidence for star formation on the smallest scales we can reach; and if so, to constrain its star formation history. Ultimately, we look at whether there are indications that the nuclear starburst and AGN are mutually influencing each other.

In §2 we describe the sample selection, observations, data reduction, PSF estimation, and extraction of the emission and absorption line morphologies and kinematics. In §3 we discuss the observational diagnostics and modelling tools. Brief analyses of the relevant facets of our new data for the individual objects are provided in Appendix A, where we also summarise results of our previously published data, re-assessing them where necessary to ensure that all objects are analysed in a consistent manner. The primary aims of our paper are addressed in §4 and §5. In §4 we discuss global results concerning the existence and recent history of nuclear star formation for our whole sample. In §5 we discuss the implications of nuclear starbursts on the starburst-AGN connection. Finally, we present our conclusions in §6.

2. Sample, Observations, Data Processing

2.1. Sample Selection

The AGN discussed in this paper form a rather heterogeneous group. They include type 1 and type 2 Seyferts, ULIRGs, and even a QSO, and do not constitute a complete sample. In order to maximise the size of the sample, we have combined objects on which we have already published adaptive optics near infrared spectra with new observations of additional targets.

Source selection was driven largely by technical considerations for the adaptive optics (AO) system, namely having a nucleus bright and compact enough to allow a good AO correction. This is actually a strength since it means that 7 of the 9 AGN are in fact broad line objects – as given either by the standard type 1 classification or because there is clear broad (FWHM $> 1000\,\mathrm{km\,s^{-1}}$) Br$\gamma$ emission in our spectra. Fig. 1 shows broad Brγ in K-band spectra of 3 AGN that are not usually classified as broad line galaxies. This is in contrast to most other samples of AGN for which star formation has been studied in detail, and avoids any bias that might arise from selecting only type 2 Syeferts. That there may be a bias arises from the increasing evidence that the obscuration in perhaps half of type 2 AGN lies at kpc scales rather than in the nucleus, which may be caused by spatially extended star formation in the galaxy disk (Brand et al. 2007; Martinez-Sansigre et al. 2006; Rigby et al. 2006). Such AGN do not fit easily into the standard unification scheme (and perhaps should not really be considered type 2 objects). Because broad lines can be seen in the infrared, we know that we are seeing down to the nuclear region and hence our results are not subject to any effects that this might otherwise introduce.

It is exactly broad line AGN for which little is known about the nuclear star formation, because the glare of the AGN swamps any surrounding stellar light in the central arcsec. As a result, most studies addressing star formation close to AGN have focussed on type 2 Seyferts. Adaptive optics makes it possible to confine much of the AGN's light into a very compact region, and to resolve the stellar continuum around it. The use of adaptive optics does give rise to one difficulty when attempting to quantify the results in a uniform way, due to the different resolutions achieved – which is a combination of both the distance to each object (i.e. target selection) and the AO performance. As a result, the standard deviation around the logarithmic mean resolution of our sample (excluding NGC 2992, see Section A) of 22 pc is a factor of 3. However, this has enabled us to study the centers of AGN across nearly 3 orders of magnitude in spatial scale, from 1 kpc in the more distant objects to only a few parsecs in the nearby objects with the best AO correction.

2.2. Observations & Reduction

A summary of our observations is given in Table 1. A description of observations and processing of the new data is given below.

Data for IRAS 05189-2524 and NGC 1068 were taken in December 2002 at the VLT with NACO, an adaptive optics near infrared camera and long slit spectrograph (Lenzen et al. 2003; Rousset et al. 2003). Since IRAS 05189-2524 is nearly face on, there is no strongly preferred axis and the slit was oriented north-south; for NGC 1068 two orientations were used, north-south and east-west. In all cases the slit width was 0.086″, yielding a nominal resolution of $R \sim 1500$ with the wide-field camera (pixel scale 0.054″) and medium resolution grism. The galaxy was nodded back and forth along the slit by 10″ to allow sky subtraction. For IRAS 05189-2524, 12 integrations of 300 sec were made; for NGC 1068 12 integrations of 300 sec were made at one position angle, and 14 frames of 200 sec at the other. All data were reduced and combined, using

standard longslit techniques in IRAF, to make the final H-band spectrum.

Data for NGC 7469, NGC 2992, NGC 1097, NGC 1068, and NGC 3783 were taken during 2004–2005 at the VLT with SINFONI, an adaptive optics near infrared integral field spectrograph (Eisenhauer et al. 2003; Bonnet et al. 2004). Data were taken with various gratings covering the H and K bands either separately ($R \sim 4000$) or together ($R \sim 1500$). The pixel scales were $0.125'' \times 0.25''$ or $0.05'' \times 0.1''$, depending on the trade-offs between field of view, spatial resolution, and signal-to-noise ratio. Individual exposure times are in the range 50–300 sec depending on the object brightness. Object frames were interspersed with sky frames, usually using the sequence O-S-O-O-S-O, to facilitate background subtraction. The data were processed using the dedicated *spred* software package (Abuter et al. 2006), which provides similar processing to that for longslit data but with the added ability to reconstruct the datacube. The data processing steps are as follows. The object frames are pre-processed by subtracting sky frames, flatfielding, and correcting bad pixels (which are identified from dark frames and the flatfield). The wavemap is generated, and edges and curvature of the slitlets are traced, all from the arclamp frame. The arclamp frame is then reconstructed into a cube, which is checked to ensure that the calibration is good. The pre-processed object frames are then also reconstructed into cubes, spatially shifted to align them using the bright nucleus as a reference, and combined. In some cases the final cube was spatially smoothed using a 3×3 median filter. Estimation of the spatial resolution (see below) was always performed after this stage.

In some cases, the strong near-infrared OH lines did not subtract well. With longer exposure times this is to be expected since the timescale for variation of the OH is only 1–2 mins. If visual inspection of the reconstructed cubes showed signs of over- or under-subtraction of the OH lines, these cubes were reprocessed using the method described in Davies (2007a).

Standard star frames are similarly reconstructed into cubes. Telluric correction and flux calibration were performed using B stars (K-band) or G2V stars (H-band). In addition, flux calibration was cross-checked in $3''$ apertures using 2MASS data, and in smaller 1–$3''$ apertures using broad-band imaging from NACO or HST NICMOS. Agreement between cubes with different pixel scales, and also with the external data, was consistent to typically 20%.

2.3. PSF Estimation

There are a multitude of ways to derive the point spread function (PSF) from adaptive optics data, five of which are described in Davies (2007b). With AGN, it is usually possible to estimate the PSF from the science data itself, removing any uncertainty about spatial and temporal variations of the PSF due to atmospheric effects. Typically one or both of the following methods are employed on the new data presented here. If a broad emission line is detected, this will always yield a measure of the PSF since the BLR of Seyfert galaxies has a diameter that can be measured in light days. Alternatively, the non-stellar continuum will provide a sufficiently good approximation in all but the nearest AGN since at near infrared wavelengths it is expected to originate from a region no more than 1–2 pc across.

In every case we have fit an analytical function to the PSF. Since the Strehl ratio achieved is relatively low, even a Gaussian is a good representation. We have used a Moffat function, which achieves a better fit because it also matches the rather broad wings that are a characteristic of partial adaptive optics correction. The PSF measured for NGC 3227, which is shown in Fig. 1 of Davies et al. (2006), can be considered typical. If one applies the concept of 'core plus halo' to this PSF, then the Gaussian fit would represent just the core while the Moffat fit the entire 'core plus halo'. Integrating both of these functions indicates that about 75%

of the flux is within the 'core', and it is thus this component which dominates the PSF. In this paper, a more exact representation of the PSF is not needed since we have not performed a detailed kinematic analysis, and we have simply used the Moffat to derive a FWHM for the spatial resolution. The resolutions achieved are listed in Table 1.

2.4. Emission/Absorption Line Characterisation

The 2D distribution of emission and absorption features has been found by fitting a function to the continuum-subtracted spectral profile at each spatial position in the datacube. The function was a convolution of a Gaussian with a spectrally unresolved template profile – in the case of emission lines it was an OH sky emission line, and for stellar absorption features we made use of template stars observed in the same configuration (pixel scale and grism). A minimisation was performed in which the parameters of the Gaussian were adjusted until the convolved profile best matched the data. During the minimisation, pixels in the data that consistently deviated strongly from the data were rejected. The uncertainties were boot-strapped using Monte Carlo techniques, assuming that the noise is uncorrelated and the intrinsic profile is well represented by a Gaussian. The method involves adding a Gaussian with the derived properties to a spectral segment that exhibits the same noise statistics as the data, and refitting the result to yield a new set of Gaussian parameters. After repeating this 100 times, the standard deviation of the center and dispersion were used as the uncertainites for the velocity and line width.

The kinematics were further processed using kinemetry (Krajnović et al. 2006). This is a parameterisation (i.e. a mathematical rather than a physical model) of the 2D field. As such, beam smearing is not a relevant issue to kinemetry, which yields an analytical expression for the observed data. Of course, when the coefficients of this expression are interpreted or used to constrain a physical model, then beam smearing should be considered. Mathematically, the kinemetry procedure fits the data with a linear sum of sines and cosines with various angular scalings around ellipses at each radius. We have used it for 3 purposes: to determine the best position angle and axis ratio for the velocity field, to remove high order noise from the raw kinematic extraction, and to recover the velocity and dispersion radial profiles. In all of the cases considered here, the kinematic centre of the velocity field was assumed to be coincident with the peak of the non-stellar continuum. In addition, the uniformity of the velocity field permitted us to make the simplifying assumption of a single position angle and axis ratio – i.e. there is no evidence for warps or twisted velocity contours. We then derived the position angle and inclination of the disk by minimising the *A1* and *B3* parameters respectively (see Krajnović et al. 2006 for a description of these). The rotation curves were recovered by correcting the measured velocity profile for inclination. We have assumed throughout the paper that the dispersion is isotropic, and hence no inclination correction was applied to the dispersion that was measured.

The innermost parts of the kinematics derived as above are of course still affected by beam smearing. In general, the central dispersion cannot necessarily be taken at face value since it may either be artificially increased by any component of rotation included within the beam size, or decreased if neighbouring regions within the beam have a lower dispersion. In the galaxies we have studied, there are two aspects which mitigate this uncertainty: the rotation speed in the central region is much less than the dispersion and so will not significantly alter it; and when estimating the central value we consider the trend of the dispersion from large radii, where the effect of the beam is small, to the center. For the basic analyses performed here, we have therefore adopted the central dispersion at face value. More detailed physical models for the nuclear disks, which properly account for the effects of beam smearing, will be presented in future publications. Lastly, we emphasize that the impact of the finite beam size on the derived rotation curve does not affect

our measurement of the dynamical mass. The reason is that, for all the dynamical mass estimates we make, the mass is estimated at a radius much large than the FWHM of the PSF – as can be seen in the relevant figures.

3. Quantifying the Star Formation

In this section we describe the tools of the trade used to analyse the data, and which lead us to the global results presented in Section 4. Specific details and analyses for individual objects can be found in Appendix A. We use the same methods and tools for all the objects to ensure that all the data are analysed in a consistent manner.

Perhaps the most important issue is how to isolate the stellar continuum, which is itself a powerful diagnostic. In addition, we use three standard and independent diagnostics to quantify the star formation history and intensity in the nuclei of these AGN. These are the Brγ equivalent width, supernova rate, and mass-to-light ratio. Much of the discussion concerns how we take into account the contribution of the AGN when quantifying these parameters. We also consider what impact an incorrect compensation could have on interpretation of the diagnostics.

We model these observational diagnostics using the stellar population and spectral synthesis code STARS (e.g. Sternberg 1998; Sternberg et al. 2003; Förster Schreiber et al. 2003; Davies et al. 2003, 2005). This code calculates the distribution of stars in the Hertzsprung-Russell diagram as a function of age for an assumed star formation history. We usually assume an exponentially decaying star formation rate, which has an associated timescale τ_{SF}. Spectral properties of the cluster are then computed given the stellar population present at any time. We note that the model output of STARS is quantitatively similar to that from version 5.1 of Starburst99, which unlike earlier versions does include AGB tracks (Leitherer et al. 1999; Vazquez & Leitherer 2005). As discussed in detail below, particular predictions of STARS include, for ages greater than 10 Myr: equivalent widths of $W_{\mathrm{CO2-0}} \sim 12\mathring{A}$ and $W_{\mathrm{CO6-3}} \sim 4.5\mathring{A}$, and H-K color of 0.15 mag. The equivalent quantities predicted by Starburst99 v5.1 are $W_{\mathrm{CO2-0}} \sim 11\mathring{A}$ and $W_{\mathrm{CO6-3}} \sim 5\mathring{A}$, and H-K color of 0.2 mag.

3.1. Isolating the stellar continuum

For small observational apertures a significant fraction of the K-band (and even H-band) continuum can be associated with non-stellar AGN continuum. The AGN contribution can be estimated from a simple measurement of the equivalent width of a stellar absorption feature. We use CO 2-0 2.29μm in the K-band or CO 6-3 1.62μm in the H-band. Although the equivalent widths $W_{\mathrm{CO2-0}}$ and $W_{\mathrm{CO6-3}}$ vary considerably for individual stars, the integrated values for stellar clusters span only a rather limited range. This was shown by Oliva et al. (1995) who measured these values for elliptical, spiral, and star-forming (HII) galaxies. We have plotted their measurements of these two absorption features in the left-hand panel of Fig. 2, together with the equivalent widths of giant and supergiant stars from Origlia et al. (1993).

In STARS we use empirically determined equivalent widths from library spectra (Förster Schreiber 2000) to compute the time-dependent equivalent width for an entire cluster of stars. Results for various star formation histories are shown in the centre and right panels of Fig. 2, for $W_{\mathrm{CO6-3}}$ and $W_{\mathrm{CO2-0}}$ respectively. Typical values are $W_{\mathrm{CO6-3}} = 4.5\mathring{A}$ and $W_{\mathrm{CO2-0}} = 12\mathring{A}$. The dashed box in the left panel shows that the

locus of 20% deviation from each of these computed values is consistent with observations. That the H\textsc{ii} galaxies have slightly higher $W_{\rm CO2-0}$ can be understood because these are selected to have bright emission lines and hence are strongly biassed towards young stellar ages – often corresponding to the maximum depth of the stellar features that occurs at $10\,\rm Myr$ due to the late-type supergiant population. It may be this bias for galaxies selected as 'starbursts', and the similarity of the CO depth for starbursts of all other ages, that led Ivanov et al. (2000) to conclude that there is no evidence for strong starbursts in Seyfert 2 galaxies. Similarly, an estimate of the dilution can be found from the Na\textsc{i} 2.206μm line. Fig. 7 of Davies et al. (2005) shows that for nearly all star formation histories the value $W_{\rm Na\,I}$ remains in the range 2–3Å.

Our conclusion here is that within a reasonable uncertainty of $\pm20\%$ (see Fig. 2), one can assume that the intrinsic equivalent width of the absorption – most notably CO – features of any stellar population that contains late-type stars is independent of the star formation history and age. For a stellar continuum diluted by additional non-stellar emission, the fraction of stellar light is

$$f_{\rm stellar} = W_{\rm obs}/W_{\rm int}$$

where $W_{\rm obs}$ and $W_{\rm int}$ are the observed and intrinsic equivalent widths of the CO features discussed above. Thus, we are able to correct the observed continuum magnitude for the contribution associated with the AGN.

3.2. Stellar colour and luminosity

Our data cover both the H and K-bands – hence the reason for using both $W_{\rm CO6-3}$ and $W_{\rm CO2-0}$. In order to homogenize the dataset, we need to convert H-band stellar magnitudes to K-band. The STARS computation in Fig. 3 shows that this conversion is also independent of the star formation history, being close to $H - K = 0.15\,\rm mag$ (no extinction) for all timescales and ages. This result is supported empirically by photometry of elliptical and spiral galaxies performed by Glass (1984). For ellipticals $H - K \sim 0.2$–0.25, and for spirals $H - K \sim 0.2$–0.3. Some of the difference between the data and models could be due to extinction since $H - K = (H - K)_0 + (A_H - A_K)$; and for $A_V = 1$, $A_H - A_K = 0.08$. However, at the level of precision required here, the 5–10% difference between model and data can be considered negligible.

To convert from absolute magnitude to luminosity we use the relation

$$M_K = -0.33 - 2.5\log L_K$$

where L_K is the total luminosity in the 1.9–2.5μm band in units of bolometric solar luminosity ($1\,L_\odot = 3.8 \times 10^{26}\,\rm W$), and as such different from the other frequently used monochromatic definition with units of the solar K-band luminosity density ($2.15 \times 10^{25}\,\rm W\,\mu m^{-1}$). We then use STARS to estimate the bolometric stellar luminosity $L_{\rm bol}$. The relation between $L_{\rm bol}$ and L_K is shown in the right panel of Fig. 3. The dimensionless ratio $L_{\rm bol}/L_K$ depends on the age and the exponential decay timescale of the star formation. However, the range spanned is only 20–200 for ages greater than $10\,\rm Myr$. Thus even if the star formation history cannot be constrained, a conversion ratio of $L_{\rm bol}/L_K \sim 60$ will have an associated uncertainty of only $0.3\,\rm dex$. In general we are able to apply constraints on the star formation age, and so our errors will be accordingly smaller.

3.3. Specific Star Formation Diagnostics

Graphs showing how the diagnostics vary with age and star formation timescale are shown in Fig. 4.

3.3.1. Brγ equivalent width

Once the stellar continuum luminosity is known, an upper limit to the equivalent width of Brγ asssociated with star formation can be found from the narrow Brγ line flux. In some cases it is possible to estimate what fraction of the narrow Brγ might be associated with the AGN. This can be done both morphologically, for example if the line emission is extended along the galaxy's minor axis; and/or kinematically, for example if the line shows regions that are broader, perhaps with FWHM a few hundred $km\,s^{-1}$, suggestive of outflow. Even if acounting for the AGN contribution is not possible, one may be able to set interesting upper limits or even rule out continuous star formation scenarios, and put a constraint on the time since the star formation was active. This can be seen in the lefthand panel of Fig. 4, which shows for example that for ages less than 10^9 yrs, continuous star formation scenarios will always have $W_{Br\gamma} > 12\,$Å.

3.3.2. Supernova rate

We estimate the type II (core collapse) supernova rate ν_{SN} from the radio continuum using the relation (Condon 1992):

$$L_N(W\ Hz^{-1}) \ = \ 1.3 \times 10^{23}\ \nu^{-\alpha}(GHz)\ \nu_{SN}(yr^{-1})$$

where L_N is the non-thermal radio continuum luminosity, ν is frequency of the observation and $\alpha \sim 0.8$ the spectral index of the non-thermal continuum. This relation was derived for Galactic supernova remnants; but a similar one, differing only in having a coefficient of 1.1×10^{23}, was derived by Huang et al. (1994) for M 82. For the 5 GHz non-thermal radio continuum luminosity of Arp 220 (176 mJy, Anantharamaiah et al. 2000) it would lead to a supernova rate of $2.9\,yr^{-1}$, comfortably within the 1.75–$3.5\,yr^{-1}$ range estimated by Smith et al. (1998) based on the detection of individual luminous radio supernovae. This, therefore, seems a reasonable relation to apply to starbursts.

We have to be careful, however, to take into account any contribution from the AGN to the radio continuum. Our premise for the nuclei of Seyfert galaxies is that if the nuclear radio continuum is spatially resolved (i.e. it has a low brightness temperature) and does not have the morphology of a jet, it is likely to originate in extended star formation. At the spatial scales of a few parsec or more that we can resolve, emission from the AGN will be very compact. As a result, we can use the peak surface brightness to estimate the maximum (unresolved) contribution from an AGN. Wherever possible, we use radio continuum observations at a comparable resolution to our data to derive the extended emission; and observations at higher resolution to estimate the AGN contribution. Details of the data used in each case are given in the relevant sub-sections for each object in Appendix A. In addition, we exclude any emission obviously associated with jets, for example as in NGC 1068.

To use ν_{SN} as a diagnostic, we normalise it with respect to the stellar K-band luminosity. This gives the ratio $10^{10}\nu_{SN}/L_K$, for which STARS output is drawn in Fig. 4.

3.3.3. Mass-to-light ratio

Models indicate that the ratio M/L_K of the stellar mass to K-band luminosity should be an excellent diagnostic since, for ages greater than 10 Myr, it increases monotonically with age as shown in Fig. 4.

However, in practice estimating the stellar mass is not entirely straightforward. In many cases it is only practicable to derive the dynamical mass. It may be possible to estimate and hence correct for the molecular gas mass based on millimetre CO maps, but these are scarce at sufficiently high spatial resolution and are associated with their own CO-to-H_2 conversion uncertainties. We also note that it is often not possible to separate the 'old' and 'young' stellar populations. The best one can do is estimate the overall mass-to-light ratio, and argue that this is an upper limit to the true ratio for the young population. While there inevitably remains uncertainty on the true ratio, the limit is often sufficient to apply useful constraints on the age of the 'young' population.

Our estimates of the dynamical mass are based wherever possible on the stellar kinematics, since the gas kinematics can be perturbed by warps, shocks, and outflows. We begin by estimating the simple Keplerian mass assuming that the stars are supported by ordered rotation at velocity $V_{\rm rot} = V_{\rm obs}/\sin i$ in a thin plane. However, the stellar kinematics in all the galaxies exhibit a significant velocity dispersion indicating that a considerable mass is supported by random rather than ordered motions. Thus the simple Keplerian mass is very much an underestimate, and any estimate of the actual mass is associated with large uncertainties – see for example Bender et al. (1992), who derive masses of spheroidal systems. As stated in Section 2, we assume that the random motions are isotropic. Our relation for estimating the mass enclosed within a radius R is then

$$M = (V_{\rm rot}^2 + 3\sigma^2)R/G.$$

where σ is the observed 1-dimensional velocity dispersion.

We note that when taking rotation into account in estimating the masses of spheroids with various density profiles, Bender et al. (1992) also use a factor 3 between the V and σ terms in their Appendix B. Despite the complexities involved, within the unavoidable uncertainties (a factor 2–3), their relation gives the same mass as that above. Although this uncertainty appears to be quite large, it does not impact the results and conclusions in this paper since we are concerned primarily with order-of-magnitude estimates when considering mass surface densities.

4. Properties of Nuclear Star Formation

In the following section we bring to together the individual results (detailed in Appendix A) to form a global picture. It is possible to do this because all the data have been analysed in a consistent manner, using the tools described in Section 3 to compare in each object the same diagnostics to the same set of stellar evolutionary synthesis models.

We note that the discussion that follows is based on results for 8 of the AGN we have observed. As explained in Appendix A we exclude NGC 2992 because we are not able to put reliable constraints on the properties of the nuclear star formation. Despite this, there are indications that at higher spatial resolution one should expect to find a distinct nuclear stellar population as has been seen in other AGN.

Size scale   Tracing the stellar features rather than the broad-band continuum, we have in all cases resolved a stellar population in the nucleus close around the AGN. While this should not be unexpected if the stellar distribution follows a smooth $r^{1/4}$ or exponential profile, we have in several cases been able to show that on scales of $< 50\,\mathrm{pc}$ there is in fact an excess above what one would expect from these profiles. This suggests that in general we are probing an inner star forming component.

Fig. 5 shows normalised azimuthally averaged stellar luminosity profiles for the AGN. These have not been corrected for a possible old underlying population, nor has any deconvolution with the PSF been performed. Nevertheless, it is still clear that the stellar intensity increases very steeply towards the nucleus. In 6 of the 8 galaxies shown, the half-width at half-maximum is less than $50\,\mathrm{pc}$. The remaining 2 galaxies are the most distant in the sample, and the spatial resolution achieved does not permit a size measurement on these scales. We may conclude that the physical radial size scale of the nuclear star forming regions in Seyfert galaxies does not typically exceed $50\,\mathrm{pc}$.

Stellar Age   For 8 of the AGN studied here, we have been able to use classical star formation diagnostics based on line and continuum fluxes as well as kinematics to constrain the ages of the inner star forming regions. The resulting ages should be considered 'characteristic', since in many cases there may simultaneously be two or more stellar populations that are not co-eval. For example, if a bulge population exists on these small spatial scales, it was not usually possible to account for the contamination it would introduce. While this would have little effect on $W_{\mathrm{Br}\gamma}$, it could impact on M/L_{K} more strongly, increasing the inferred age. The ages we find lie in the range 10–300 Myr, compelling evidence that it is common for there to be relatively young star clusters close around AGN.

Intriguingly, we also find rather low values of $W_{\mathrm{Br}\gamma}$: typically $W_{\mathrm{Br}\gamma} \lesssim 10\,\text{Å}$ (see Table 3). This indicates directly that there is currently little or no on-going star formation. Coupled with the relatively young ages, we conclude that the star formation episodes are short-lived. One may speculate then that the star formation is episodic, recurring in short bursts. The scale of the bursts and time interval between them would certainly have an impact on the fraction of Seyfert nuclei in which observational programmes are able to find evidence for recent star formation.

Nuclear Stellar Disks   The first evidence for nuclear stellar disks came from seeing limited optical spectroscopy, for which a slight reduction in σ_* was seen for some spiral galaxies (Emsellem et al. 2001; Márquez et al. 2003; Shapiro et al. 2003). And there is now a growing number of spiral galaxies – more than 30 – in which the phenomenon has been observed, suggesting that they might occur in 30% or more of disk galaxies (Emsellem 2006c). The σ_*-drop has been interpreted by Emsellem et al. (2001) as arising from a young stellar population that is born from a dynamically cold gas component, and which makes a significant contribution to the total luminosity. This appears to be borne out by N-body and SPH simulations of isolated galaxies (Wozniak et al. 2003), which suggest that although the entire central system will slowly heat up with time, the σ_*-drop can last for at least several hundred Myr. Indeed, preliminary analysis of optical integral field data for NGC 3623 suggest that the stellar population responsible for the σ_*-drop cannot be younger than 1 Gyr (Emsellem 2006b).

Our results provide strong support for the nuclear disk interpretation. In previous work (Davies et al. 2006; Mueller Sánchez et al. 2006), we had argued that in both Circinus and NGC 3227 the inner distributions were disk-like, albeit thickened. We have now found much more direct evidence for this phenomenon in NGC 1097 and NGC 1068. In both of these galaxies, we have spatially resolved a σ_*-drop and an excess

stellar continuum over the same size scales. In NGC 1097 this size was $\sim 0.5''$, corresponding to about 40 pc. For NGC 1068 these effects were measured out to $\sim 1''$, equivalent to 70 pc. These are not the scale lengths of the disks, but simply the maximum radius to which we can detect them. In both cases the mean mass surface densities are of order $\Sigma = (1\text{-}3) \times 10^4 \, \mathrm{M_\odot \, pc^{-2}}$. For an infinitely large thin self gravitating stellar disk, one can use the expression $\sigma_z^2 = 2\pi G \Sigma z_0$ to estimate the scale height. Although this may not be entirely appropriate, we use it here to obtain a rough approximation to the scale heights, which are 5–20 pc. Thus while the disks appear to be flattened, they should still be considered thick since the radial extent is only a few times the scale height.

The impact of nuclear starbursts on the central light profile of galaxies was considered theoretically more than a decade ago by Mihos & Hernquist (1994). They performed numerical simulations of galaxy mergers to study the mass and luminosity profiles of the remnants, taking gas into account, and estimating the star formation rate using a modified Schmidt law. They found that there should be a starburst in the nucleus which would give rise to an excess stellar continuum above the $r^{1/4}$ profile of the older stars in the merged system. Several years ago, compact nuclei were found to be present in a significant fraction of spiral galaxies (Balcells et al. 2003) as well as Coma cluster dwarf ellipticals (Graham & Guzmán 2003). More recently, nuclei with a median half-light radius of 4.2 pc have been found in the majority of early-type members of the Virgo Cluster (Côté et al. 2006); and traced out to $\sim 1''$, equivalent to ~ 100 pc, in some of the 'wet' merger remnants in that cluster (Kormendy et al. 2007). While the nuclear starbursts in these latter cases are caused by a merger event, whereas those we are studying arise from secular evolution as gas from the galaxy disk accretes in the nucleus, there appear to be many parallels in the phenomenology of the resulting starbursts.

Star Formation Rate It is possible to estimate the bolometric luminosity $L_{\mathrm{bol*}}$ of the stars from their K-band luminosity L_{K} even if one knows nothing about the star formation history. As discussed in Section 3, this would result in an uncertainty of about a factor 3. The diagnostics in Table 3 and discussions in Appendix A enable us to apply some constraints to the characteristic age of the star formation. Because continuous star formation is ruled out by the low $W_{\mathrm{Br}\gamma}$, we have assumed exponential decay timescales of $\tau_{\mathrm{SF}} = 10\text{--}100\,\mathrm{Myr}$. We have then used STARS to estimate the average star formation rates. In order to allow a meaningful comparison between the objects, the rates have been normalised to the same area of $1\,\mathrm{kpc^2}$. These are the rates given in Table 3. They are calculated simply as the mass of stars produced divided by the entire time since the star forming episode began. Because τ_{SF} is shorter than the age, the average includes both active and non-active phases of the starburst. Indeed, for $\tau_{\mathrm{SF}} = 10\,\mathrm{Myr}$ one would expect the star formation rate during the active phases to be at least a factor of a few, and perhaps an order of magnitude, greater. The table shows that on scales of a few hundred parsecs one might expect a few $\times 10\,\mathrm{M_\odot \, yr^{-1} \, kpc^{-2}}$, while on scales of a few tens of parsecs mean rates reaching $\sim 100\,\mathrm{M_\odot \, yr^{-1} \, kpc^{-2}}$ should not be unexpected; and correspondingly higher – up to an order of magnitude, see Fig. 6 – during active phases.

An obvious question is why there should be such vigorous star formation in these regions. Star formation rates of $10\text{--}100\,\mathrm{M_\odot \, yr^{-1} \, kpc^{-2}}$ are orders of magnitude above those in normal galaxies and comparable to starburst galaxies. The answer may lie in the Schmidt law and the mass surface densities we have estimated in Table 3. Fig. 7 shows these surface densities at the radii over which they were estimated, revealing a trend towards higher densities on smaller scales and values of a few times $10^4 \, \mathrm{M_\odot \, pc^{-2}}$ in the central few tens of parsecs. The global Schmidt law, as formulated by Kennicutt (1998), states that the star formation rate depends on the gas surface density as $\Sigma_{\mathrm{SFR}} \propto \Sigma_{gas}^{1.4}$. If one assumes that 10–30% of the mass in our AGN is

gas, then this relation would predict time-averaged star formation rates in the range 10–$100\,\mathrm{M_\odot\,yr^{-1}\,kpc^{-2}}$, as have been observed. That the high star formation rates may simply be a consequence of the high mass surface densities is explored futher by Hicks et al. (in prep.).

Stellar Luminosity   As a consequence of the high star formation rates, the stellar luminosity per unit area close around the AGN is very high in these objects. Despite this, because the star formation is occurring only in very small regions, the absolute luminosities are rather modest. This can be seen in Fig. 8 which shows the bolometric luminosity of the stars as a fraction of the entire bolometric luminosity of the galaxy. We have calculated a range for the ratio $L_{\mathrm{bol}*}/L_{\mathrm{K}}$ appropriate for each galaxy based on the ages in Table 3 for different τ_{SF}. Because we assume that all the K-band stellar continuum is associated with the young stars, we have adopted the lower end of each range in an attempt to minimise possible overestimation of $L_{\mathrm{bol}*}$. The resulting values for the ratio used span 30–130, within a factor of 2 of the 'baseline' value of 60 given in Section 3. In the central few tens of parsecs, young stars contribute a few percent of the total. But integrated over size scales of a few hundred parsecs, this fraction can increase to more than 20%. On these scales, the star formation is energetically significant when compared to the AGN. Such high fractions imply that on the larger scales the extinction to the young stars must be relatively low. On the other hand, on the smallest scales where in absolute terms the stellar luminosity is small, there could in general be considerable extinction even at near infrared wavelengths. In this paper we have not tried to account for extinction since it is very uncertain. The primary effect of doing so would simply be to increase the stellar luminosity above the values discussed here.

Fig. 9 shows the stellar bolometric luminosity $L_{\mathrm{bol}*}$ integrated as a function of radius. All the curves follow approximately the same trend, with the luminosity per unit area increasing towards smaller scales and approaching $10^{13}\,\mathrm{L_\odot\,kpc^{-2}}$ in the central few parsecs. This appears to be a robust trend and will not change significantly even with large uncertainties of a factor of a few. It is remarkable that the luminosity density of $10^{13}\,\mathrm{L_\odot\,kpc^{-2}}$ is that estimated by Thompson et al. (2005) for ULIRGs, which they modelled as optically thick starburst disks. The main difference between the ULIRG model and the starbursts close around AGN is the spatial scales on which the starburst occurs.

Based on this model, they argued that ULIRGs are radiating at the Eddington limit for a starburst, defined as when the radiation pressure on the gas and dust begins to dominate over self-gravity. The limiting luminosity-to-mass ratio was estimated to be $\sim 500\,\mathrm{L_\odot/M_\odot}$ by Scoville (2003). He argued that in a star cluster, once the upper end of the main sequence was populated, the radiation pressure would halt further accretion on to the star cluster and hence terminate the star formation. Following Thompson et al. (2005), we apply this definition to the entire disk rather than a single star cluster. For the $10^{13}\,\mathrm{L_\odot\,kpc^{-2}}$, this implies a mass surface density of $2 \times 10^4\,\mathrm{M_\odot\,pc^{-2}}$. Comparing these quantities to the AGN we have observed, we find that on scales of a few tens of parsecs they are an order of magnitude below the Eddington limit. On the other hand, we have already seen that the low $W_{\mathrm{Br}\gamma}$ indicates that there is little on-going star formation and hence that the starbursts are short-lived. This is important because short-lived starbursts fade very quickly. As shown in Fig. 6, for a decay timescale of $\tau_{\mathrm{SF}} = 10\,\mathrm{Myr}$, $L_{\mathrm{bol}*}$ will have decreased from its peak value by more than an order of magnitude at an age of $100\,\mathrm{Myr}$. Thus it is plausible – and probably likely – that while the star formation was active, the stellar luminosity was an order of magnitude higher. In this case the starbursts would have been at, or close to, their Eddington limit at that time.

The luminosity-to-mass ratio of $500\,\mathrm{L_\odot/M_\odot}$ associated with the Eddington limit is in fact one that all young starbursts would exceed if, beginning with nothing, gas was accreted at the same rate that it was converted into stars. That, however, is not a realistic situation. A more likely scenario, shown in Fig. 10, is

that the gas is already there in the disk. In this case, a starburst with a star-forming timescale of $100\,\mathrm{Myr}$ could never exceed $100\,\mathrm{L_\odot/M_\odot}$. To reach $500\,\mathrm{L_\odot/M_\odot}$, the gas would need to be converted into stars on a timescale $\lesssim 10\,\mathrm{Myr}$. This timescale is independent of how much gas there is. Thus, for a starburst to reach its Eddington limit, it must be very efficient, converting a significant fraction of its gas into stars on very short $\sim 10\,\mathrm{Myr}$ timescales. This result is consistent with the prediction of the Schmidt law, which states that disks with a higher gas surface density will form stars more efficiently. The reason is that the star formation efficiency is simply $SFE = \Sigma_{\mathrm{SFR}}/\Sigma_{\mathrm{gas}} \propto \Sigma_{\mathrm{gas}}^{0.4}$. Thus, from arguments based solely on the Schmidt law and mass surface density, one reaches the same conclusion that the gas supply would be used rather quickly and the lifetime of the starburst would be relatively short.

Summarising the results above, a plausible scenario could be as follows. The high gas density leads to a high star formation rate, producing a starburst that reaches its Eddington limit for a short time. Because the efficiency is high, the starburst can only be active for a short time and then begins to fade. Inevitably, one would expect that the starburst is then dormant until the gas supply is replenished by inflow. This picture appears to be borne out by the observations presented here.

5. Starburst-AGN Connection

In the previous sections we have presented and discussed evidence that in general there appears to have been moderately recent star formation on small spatial scales around all the AGN we have observed. Fig. 11 shows the first empirical indication of a deeper relationship between the star formation and the AGN. In this figure we show the luminosity of the AGN, both in absolute units of solar luminosity and also in relative units of its Eddington luminosity L_{Edd}, against the age of the most recent known nuclear star forming episode. Since the AGN luminosity is not well known, we have made the conservative assumption that it is equal to half the bolometric luminosity of the galaxy – as may be the case for NGC 1068 (Pier et al. 1994, but see also Bland-Hawthorne et al. 1997). To indicate the expected degree of uncertainty in this assertion we have imposed errorbars of a factor 2 in either direction, equivalent to stating that the AGN luminosity in these specific objects is likely to be in the range 25–100% of the total luminosity of the galaxy. The Eddington luminosity is calculated directly from the black hole mass, for which estimates exist for these galaxies from reverberation mapping, the $\mathrm{M_{BH}} - \sigma*$ relation, maser kinematics, etc. These are listed in Table 2. For the age of the star formation, we have plotted the time since the most recent known episode of star formation began, as given in Table 3. For galaxies where a range of ages is given, we have adopted these to indicate the uncertainty; the mean of these, $\sim \pm 30\%$, has been used to estimate the uncertainty in the age for the rest of the galaxies. We note that these errorbars reflect uncertainties in characterising the age of the star formation from the available diagnostics and also in the star formation timescale τ_{SF}. However, there are still many implicit assumptions in this process, and we therefore caution that the actual errors in our estimation of the starburst ages may be larger than that shown.

Conceding this, we do not wish to over-interpret the figure. Keeping the uncertainties in mind, Fig. 11 shows the remarkable result that AGN which are radiating at lower efficiency $\lesssim 0.1\,\mathrm{L/L_{Edd}}$ are associated with younger $\lesssim$ 50–100 Myr starbursts; while those which are more efficient $\gtrsim 0.1\,\mathrm{L/L_{Edd}}$ have older $\gtrsim$ 50–100 Myr starbursts. If one were to add to this figure the Galactic Centre – which is known to have an extremely low luminosity ($\mathrm{L/L_{Edd}} < 10^{-5}$; Ozernoy & Genzel 1996; Baganoff et al. 2003) and to have experienced a starburst $6 \pm 2\,\mathrm{Myr}$ ago (Paumard et al. 2006) – it would be consistent with the categories above. The inference is that either there is a delay between the onset of starburst activity and the onset of AGN activity, or star formation is quenched once the black hole has become active.

In Section 4 we argued that the starbursts are to some extent self-quenching: that very high star formation efficiencies are not sustainable over long periods. In addition, an intense starburst will provide significant heat input to the gas, which is perhaps partially responsible for the typically high gas velocity dispersions in these regions (Hicks et al., in prep.). This itself could help suppress further star formation. Heating by the AGN could also contribute to this process, and has been proposed as the reason why the molecular torus is geometrically thick (Pier & Krolik 1992; Krolik 2007). It is also used to modulate star formation (at least on global scales) in semi-analytic models of galaxy evolution (Granato et al. 2004; Springel et al. 2005). While this is certainly plausible, it does not explain either why the star formation in some galaxies with a lower luminosity AGN has already ceased, nor why none of the AGN associated with younger starbursts are accreting efficiently.

Instead we argue for the former case above, that efficient fuelling of a black hole is associated with a starburst that is at least 50–100 Myr old. It may be because of such a delay between AGN and starburst activity that recent star formation is often hard to detect close to AGN: the starburst has passed its most luminous (very young) age, and is in decline while the AGN is in its most active phase (see Fig. 6). This does not necessarily imply that the *a priori* presence of a starburst is required before an AGN can accrete gas – although it seems inevitable that one will occur as gas accumulates in the nucleus. Nor does it imply that all starbursts will result in fuelling a black hole; indeed it is clear that there are many starbursts not associated with AGN. As we argue below, the crucial aspect may be the stellar ejecta associated with the starburst; and in particular, not just the mass loss rate, but the speed with which the mass is ejected.

Winds from OB stars In the Galactic Center, Ozernoy & Genzel (1996) proposed that it is the recent starburst there that is limiting the luminosity of the black hole. In this scenario, mechanical winds from young stars – both the outflow and the angular momentum of the gas (which is a consequence of the angular momentum of the stars themselves) – hinder further inflow. The authors argued that almost none of the gas flowing into the central parsec reached the black hole because of outflowing winds from IRS 16 and He I stars in that region. Detailed modelling of the Galactic Center region as a 2-phase medium was recently performed by Cuadra et al. (2006). They included both the fast young stellar winds with velocities of $700 \, \mathrm{km \, s^{-1}}$ (Ozernoy et al. 1997) and the slower winds of $\sim 200 \, \mathrm{km \, s^{-1}}$ (Paumard et al. 2001); and also took into account the orbital angular momentum of the stars (Paumard et al. 2001; Genzel et al. 2003), which had a strong influence on reducing the accretion rate. They found that the average accretion rate onto the black hole was only $\sim 3 \times 10^{-6} \, \mathrm{M_\odot \, yr^{-1}}$, although an intermittent cold flow superimposed considerable variability onto this. In contrast, the hypothetical luminosity Ozernoy & Genzel (1996) estimate that Sgr A* would have if it could accrete all the inflowing gas, would be $5 \times 10^{43} \, \mathrm{erg \, s^{-1}}$, typical of Seyfert galaxies. In principle this process could be operating in other galaxy nuclei where there has been a starburst which extends to less than 1 pc from the central black hole. However, it cannot explain the timescale of the delay we have observed, which is an order of magnitude greater than the main sequence lifetime of OB and Wolf-Rayet stars.

Winds from AGB stars Stars of a few (1–$8 \, \mathrm{M_\odot}$) solar masses will evolve on to the asymptotic giant branch (AGB) at the end of their main sequence lifetimes. The timescale for stars at the upper end of this range to reach this phase is $\sim 50 \, \mathrm{Myr}$, comparable to the delay apparent in Fig. 9. Since AGB stars are known to have high mass-loss rates, of order 10^{-7}–$10^{-4} \, \mathrm{M_\odot \, yr^{-1}}$ at velocities of 10–$30 \, \mathrm{km \, s^{-1}}$ (Winters et al. 2003), they may be prime candidates for explaining the delay between starburst and AGN activity. To quantify this, we consider how much of the mass in the wind could be accreted by the central supermassive black

hole.

The Bondi parameterisation of the accretion rate onto a point particle for a uniform spherically symmetric geometry is given by (Bondi 1952)

$$\dot{M} \;\; = \;\; \frac{2\pi\, G^2\, M^2\, \rho}{(V^2 + c_s^2)^{3/2}}$$

where M is the mass of the point particle moving through a gas cloud, V is the velocity of the particle with respect to the cloud, ρ is the density of the cloud far from the point particle, and c_s is the sound speed. This approximation is still used to quantify accretion on to supermassive black holes in models of galaxy evolution (Springel et al. 2005), even though it may be significantly inaccurate for realistic (e.g. turbulent) media (Krumholz et al. 2006). Here, it is sufficient to provide an indication of the role that stellar winds may play in accretion onto a central black hole. The density of the stellar wind at a distance R from the parent star is given by

$$\rho_{\mathrm{wind}} \;\; = \;\; \frac{\dot{M}_{\mathrm{wind}}}{4\, R^2\, V_{\mathrm{wind}}}$$

In our case, R is the distance from the star to the black hole. One would therefore expect that the accretion rate on to the black hole could be written as (see also Melia 1992)

$$\dot{M}_{\mathrm{BH}} \;\; \sim \;\; \frac{G^2\, M_{\mathrm{BH}}^2\, \dot{M}_{\mathrm{wind}}}{(V_{\mathrm{wind}}^2 + c_s^2)^{3/2}\, V_{\mathrm{wind}}\, R^2}$$

This equation shows that $\dot{M}_{\mathrm{BH}} \propto V_{\mathrm{wind}}^{-4}$. We have implicitly assumed that V_{wind} is greater than the orbital velocity V_{orb} of the star from which it originates. This is not the case for AGB winds, and so one reaches the limiting case of $\dot{M}_{\mathrm{BH}} \propto V_{\mathrm{orb}}^{-4}$, where for the galaxies we have observed $V_{\mathrm{orb}} \sim 50\text{--}100\,\mathrm{km\,s^{-1}}$. This is still at least an order of magnitude less than the winds from OB and Wolf-Rayet stars. Thus, even though the mass loss rates from individual OB and Wolf-Rayet stars are similar to those of AGB stars, the AGB winds will fuel a black hole much more efficiently. However, for slow stellar winds that originate close to a $10^7\,\mathrm{M_\odot}$ black hole, the equation breaks down because the conditions of uniformity and spherically symmetry are strongly violated. Indeed, the apparent accretion rate exceeds the outflow rate – implying that essentially the entire wind can be accreted. For AGB wind velocities of $10\text{--}30\,\mathrm{km\,s^{-1}}$, the maximum radius at which the entire wind from a star in Keplerian orbit around a $10^7\,\mathrm{M_\odot}$ black hole will not exceed the escape velocity from that orbit (i.e. $V_{\mathrm{wind}} + V_{\mathrm{orb}} < V_{\mathrm{esc}}$) is around $10\text{--}70\,\mathrm{pc}$. We adopt the middle of this range, $40\,\mathrm{pc}$, as the characteristic radius within which it is likely that a significant fraction, and perhaps most, of the AGB winds are accreted onto the black hole. Fig. 9 indicates that the stellar luminosity within this radius is $\sim 2 \times 10^9\,\mathrm{L_\odot}$. It is this luminosity that has been used to scale the STARS model (for $\tau_{\mathrm{SF}} = 10\,\mathrm{Myr}$ and an age of $100\,\mathrm{Myr}$) in Fig. 6, and so one can also simply read off the mass loss from the figure. The mass loss rate for such winds peaks at about $0.1\,\mathrm{M_\odot\,yr^{-1}}$ and then tails off proportionally to the K-band luminosity, leading to a cumulative mass lost of $2 \times 10^7\,\mathrm{M_\odot}$ after $1\,\mathrm{Gyr}$ (although most of the loss occurs actually occurs within half of this timespan). This mass loss rate is sufficient to power a Seyfert nucleus for a short time. A typical Seyfert with $\mathrm{M_{BH}} \sim 10^7\,\mathrm{M_\odot}$ requires $0.02\,\mathrm{M_\odot\,yr^{-1}}$ to radiate at the Eddington limit. Even for the short bursts we have modelled, Fig. 6 shows that this can be supplied by AGB winds for starburst ages in the range $50\text{--}200\,\mathrm{Myrs}$.

We note that taking an AGB star luminosity of $10^4\,\mathrm{L_\odot}$ (which is at the high end of the likely average, Nikolaev & Weinberg 1997) we then find that there are $\sim 2 \times 10^5$ AGB stars close enough to the black hole to contribute to accretion. In order to provide at least $0.02\,\mathrm{M_\odot\,yr^{-1}}$, the typical mass loss rate per star must

exceed $10^{-7}\,M_\odot\,\mathrm{yr}^{-1}$, which is the lower limit of the range measured for Galactic AGB stars given above. Thus the mass losses and rates estimated here appear to be plausible.

The low speed of these winds means they will not create much turbulence. We quantify this by considering their total mechanical energy $\frac{1}{2}mv^2$ integrated over the same timespan, which is $\sim 10^{45}\,\mathrm{J}$. These two quantities – gas mass ejected and mechanical energy – are compared to those for supernovae below.

Supernovae Type II supernovae are the stellar outflows most able to create turbulence in the interstellar medium, since they typically eject masses of $\sim 5\,M_\odot$ at velocities of $\sim 5000\,\mathrm{km\,s^{-1}}$ (Chevalier 1977). Each supernova therefore represents a considerable injection of mechanical momentum and energy into the local environment. A large number of compact supernova remnants are known, for example in M 82 and Arp 220, and are believed to have expanded into dense regions with $n_H \sim 10^3$–$10^4\,\mathrm{cm}^{-3}$ (Chevalier & Fransson 2001). These authors argue that such remnants become radiative when they reach sizes of $\sim 1\,\mathrm{pc}$, at which point the predicted expansion velocity will have slowed to $\sim 500\,\mathrm{km\,s^{-1}}$. By this time, the shock front will have driven across $\sim 1000\,M_\odot$ of gas. When integrated over the age of the starburst, even for low supernova rates – e.g. the current rate within 30 pc of the nucleus of NGC 3227 is $\sim 0.01\,\mathrm{yr}^{-1}$ (Davies et al. 2006) – this represents a substantial mass of gas that has been affected by supernova remnants. The STARS model we have constructed in Fig. 6 indicates that typically one could expect $\sim 10^6$ supernovae to occur as a result of one of the short-lived starbursts; and that most of these will occur around 10–50 Myr after the beginning of the starburst. For a decay timescale of the star formation rate that is longer than $\tau_{SF} = 10\,\mathrm{Myr}$, this timespan will increase. Hence, supernovae may also play a role in causing the observed delay between starburst and AGN activity.

STARS calculates the mass loss and mass loss rates using a very simple scheme, assuming that a star ejects all of its lost mass at the end of its life on a stellar track. Thus, it does not calculate the mass lost from supernovae explicitly, rather the combined mass lost from OB winds and supernovae which is much higher. We therefore adopt the $\sim 5\,M_\odot$ per supernova given above, which yields a total ejected mass of $\sim 8 \times 10^6\,M_\odot$. This is about 40% of that released by AGB winds. However, since this gas is ejected at high speed and $\dot{M}_{BH} \propto V_{wind}^{-4}$, the efficiency with which it can be accreted onto the black hole is extremely low. This can also be seen in the total mechanical energy of $\sim 10^{50}\,\mathrm{J}$, which is several orders of magnitude greater than for AGB winds. In fact the total mechanical energy exceeds the binding energy of the nuclear region, which is of order $10^{48}\,\mathrm{J}$ (assuming $10^8\,M_\odot$ within 40 pc). As a result, it is highly likely that supernova cause some fraction of the gas to be permanently expelled. Indeed, superwinds driven by starbursts are well known in many galaxies. This is not important as long as sufficient gas either remains to fuel the AGN, or more is produced by stellar winds – which, as we have argued above, appears to be the case for AGB stars.

6. Conclusions

We have obtained near infrared spectra of 9 nearby active galactic nuclei using adaptive optics to achive high spatial resolution (in several cases better than 10 pc). For 7 of these, integral field spectroscopy with SINFONI allows us to reconstruct the full 2-dimensional distributions and kinematics of the stars and gas. Although the individual AGN are very varied, we have analysed them in a consistent fashion to derive: the stellar K-band luminosity, the dynamical mass, and the equivalent width of the Brγ line. We have combined these with radio continuum data from the literature, which has been used to estimate the supernova rate. We have used these diagnostics to constrain STARS evolutionary synthesis models and hence characterize

the star formation timescales and ages of the starbursts close around AGN. Our main conclusions can be summarised as follows:

- The stellar light profiles show a bright nuclear component with a half-width at half-maximum of less than 50 pc. In a number of cases these nuclear components clearly stand out above an inward extrapolation of the profile measured on larger scales. In addition, there are 2 cases which show kinematical evidence for a distinct stellar component, indicating that the nuclear stellar populations most probably exist in thick nuclear disks. The mean mass surface densities of these disks exceeds $10^4 \, M_\odot \, pc^{-2}$.

- There is abundant evidence for recent star formation in the last 10–300 Myr. But the starbursts are no longer active, implying that the star formation timescale is short, of order a few tens of Myr. While the starbursts were active, the star formation rates would have been much higher than the current rates, reaching as high as $1000 \, M_\odot \, kpc^{-2}$ in the central few tens of parsecs (comparable to ULIRGs, but on smaller spatial scales). These starbursts would have been Eddington limited. Due to the very high star forming efficiency, the starbursts would have also exhausted their fuel supply on a short timescale and hence have been short-lived. It therefore seems likely that nuclear starbursts are episodic in nature.

- There appears to be a delay of 50–100 Myr (and in some cases perhaps more) between the onset of star formation and the onset of AGN activity. We have interpreted this as indicating that the starburst has a significant impact on fuelling the central black hole, and have considered whether outflows from stars might be responsible. While supernovae and winds from OB stars eject a large mass of gas, the high velocity of this gas means that its accretion efficiency is extremely low. On the other hand, winds from AGB stars ultimately dominate the total mass ejected in a starburst; and the very slow velocities of these winds mean they can be accreted onto the black hole very efficiently.

A.   Individual Objects

This appendix contains specific details on the individual objects. We summarize our published results from near infrared adaptive optics spectroscopy of individual objects, and present a brief analysis of the new data for several other objects. The aim of re-assessing the data for Mkn 231 that has already been published is to ensure that it is analysed using STARS in a manner that is consistent with the new data. For NGC 7469, we make a significant update of the analysis using new data from integral field spectroscopy. In general, for objects with new data, we provide only the part of the analysis relevant to understanding star formation around the AGN. Our intention is that a complete analysis for each object will be presented in future publications.

Our analyses are restricted to the nuclear region. Since there is no strict universal definition of what comprises the 'nuclear region', we explicitly state in Table 3 the size of the region we study in each galaxy. The table also presents a summary of the primary diagnostics. The way in which these have been derived, and their likely uncertainties, has been discussed in some detail already in Section 3. As such, the description of these methods is not repeated, and in this Section we discuss only issues that require special attention.

A.1. Summary of Star Forming Properties of Galaxies already Studied

A.1.1. Mkn 231

A detailed analysis of the star formation in the nucleus of Mkn 231 at a resolution of about $0.18''$ (150 pc) was given in Davies et al. (2004b). Here we summarize only the main points; no new data is presented, but the analysis is updated using STARS to make it consistent with the other objects studied in this paper.

The presence of stellar absorption features across the nucleus demonstrates the existence of a significant population of stars. The radial distribution and kinematics indicate they lie, like the gas (Downes & Solomon 1998), in a nearly face-on disk. Davies et al. (2004b) found that the dynamical mass imposed a strong constraint on the range of acceptable starburst models, yielding an upper limit to the age of the stars of around 120 Myr. Re-assessing the mass-to-light ratio using STARS models suggests that for the increased mass required by a more face-on orientation ($i = 10°$) an upper age of 250 Myr is also possible, depending on the star formation timescale. However, either a small change of only a few degrees to the inclination (to $i = 15°$), or a relatively short star formation timescale of 10 Myr would reduce the limit to the $\sim$100 Myr previously estimated. This is more consistent with the extremely high supernova rate.

The stellar luminosity, found from the dilution of the CO absorption (Davies et al. 2004b), indicates that stars within $1''$ (800 pc) of the nucleus contribute 25–40% of the bolometric luminosity of the galaxy. Similarly, within 200 pc, stars comprise 10–15% of L_{bol}. The age, star formation rate, and size scale (disk scale length of $0.18–0.2''$) are all consistent with high resolution radio continuum imaging (Carilli et al. 1998).

A.1.2. Circinus

Star formation in the central 16 pc of Circinus was addressed by Mueller Sánchez et al. (2006). The diagnostics given in Table 3 are taken from this reference. We used the depth of the CO 2-0 bandhead to estimate the stellar luminosity, combined with the narrow Brγ flux (which we argued originated in star forming regions rather than the AGN narrow line region) and the radio continuum, to constrain starburst models. The conclusion was that the starburst was less than 80 Myr old and was already decaying. On these scales it contributes 1.4% of L_{bol}, or more if extinction is considered. A similar nuclear star formation intensity was estimated by Maiolino et al. (1998), who were also able to study Circinus on larger scales. They found that the luminosity of young stars within 200 pc of the AGN was of order $10^{10} L_{\odot}$, and hence comparable to the AGN.

A.1.3.   NGC 3227

An analysis similar to that for Circinus was performed on NGC 3227 by Davies et al. (2006), and the diagnostics given in Table 3 are taken from this reference. In this case we were able to make estimates of and correct for contributions of: (1) the narrow line region to Brγ, because there were clear regions along the minor axis that had higher dispersion; (2) the AGN to the radio continuum, by estimating the maximum contribution from an unresolved source; and (3) the bulge stars to the stellar luminosity, by extrapolating the radial profile of the bulge to the inner regions. The STARS models yielded the result that in the nucleus, star formation began approximately 40 Myr ago and must have already ceased. At the resolution of 0.085″, the most compact component of stellar continuum had a measured FWHM of 0.17″, suggesting an intrinsic size scale of ~ 12 pc. Young stars within 30 pc of the AGN (i.e. more than just the most compact region) have a luminosity of $\sim 3 \times 10^9 \, L_\odot$, which is $\sim 20\%$ of the entire galaxy.

A.2.   Star Forming Properties of Galaxies with New Data

A.2.1.   NGC 7469

Star formation on large scales in NGC 7469 has been studied by Genzel et al. (1995). They found that within 800 pc of the nucleus, a region that includes the circumnuclear ring, the luminosity from young stars was $\sim 3 \times 10^{11} \, L_\odot$, about 70% of the galaxy's bolometric luminosity. This situation is similar to that in Mkn 231. On smaller scales, the nuclear star formation in NGC 7469 was directly resolved by Davies et al. (2004a) on a size scale of 0.15–0.20″ (50–65 pc) FWHM. An analysis of the longslit data, similar to that for Mkn 231, was made – making use of stellar absorption features, kinematics, and starburst models. We estimated that the age of this region was no more than 60 Myr under the assumption that the fraction of stellar light in the K-band in the central 0.2″ was 20–30%. Our new integral field SINFONI observations of NGC 7469 at a spatial resolution of 0.15″ (measured from both the broad Brγ and the non-stellar continuum profiles, see Section 2) are used here to make a more accurate estimate of the nuclear K-band luminosity. They enable us to provide a short update to the detailed analysis in Davies et al. (2004a).

The SINFONI data show that the equivalent width of the 2.3μm CO 2-0 is $W_{\mathrm{CO}\,2-0} = 1.8$Å in a 0.8″ aperture and 0.9Å in a 0.2″ aperture. The corresponding K-band magnitudes are $K = 10.4$ and $K = 11.8$ respectively. If one takes the intrinsic equivalent width of the 2.3μm CO 2-0 bandhead to be 12Å (see Section 3), one arrives at a more modest value of 8% for the stellar fraction of K-band continuum in the 0.2″ aperture. The stellar K-band luminosity in this region is then $6 \times 10^7 \, L_\odot$. Comparing this to the dynamical mass in Davies et al. (2004a) yields a mass-to-light ratio of $M/L_K \sim 0.6 \, M_\odot/L_\odot$. Previously, extrapolation from a 37 mas slit to a filled aperture had led to an underestimation of the total magnitude but an overestimation of the stellar contribution. Fortuitously, these uncertainties had compensated each other. The same analysis for the 0.8″ aperture yields a K-band stellar luminosity of $3 \times 10^8 \, L_\odot$ and hence $M/L_K \sim 1.6 \, M_\odot/L_\odot$.

The K-band datacube yields estimates of the upper limit to $W_{\mathrm{Br}\gamma}$ of 17Å and 11Å in 0.2″ and 0.8″ apertures respectively. This has been corrected for dilution of the stellar continuum (as described in Section 3) but not for a possible contribution to the narrow Brγ from the AGN. Hence the actual $W_{\mathrm{Br}\gamma}$ corresponding to only the stellar line and continuum emission will be less than these values – indicating that the star formation is unlikely still to be on-going.

We estimate the age of the star formation using the STARS models in Fig. 4. Within the 0.2″ aperture

this gives 100 Myr, comparable to our original estimate. Such a young age is supported by radio continuum measurements. With a $0.2''$ beam, Colina et al. (2001) reported that the unresolved core flux in NGC 7469 was 12 mJy at 8.4 GHz. With much higher spatial resolution of $0.03''$, Sadler et al. (1995) reported an upper limit to the unresolved 8.4 GHz continuum of 7 mJy. We assume that the difference of 5 mJy is due to emission extended on scales of 10–60 pc which is resolved out of one beam but not the other. As discussed in Section 3, star formation is a likely candidate for such emission. In this case, we would estimate the supernova rate to be $\sim 0.1\,\mathrm{yr}^{-1}$ and the ratio $10^{10}\,\nu_{\mathrm{SN}}/L_K \sim 3$. This is likely to be a lower limit since there was only an upper limit on the core radio flux density. For a ratio of this order, even allowing for some uncertainty, Fig 4 implies an age consistent with no more than 100 Myr.

Within the $0.8''$ aperture, which we adopt in Table 3, continuous star formation is inconsistent with $\mathrm{W}_{\mathrm{Br}\gamma}$. For a star formation timescale of $\tau_{\mathrm{SF}} = 100\,\mathrm{Myr}$, the mass-to-light ratio implies an age of 190 Myr, just consistent with the measured value of $\mathrm{W}_{\mathrm{Br}\gamma} = 11\text{Å}$. If some of the narrow Brγ is associated with the AGN rather than star formation, then a shorter star formation timescale is required. For $\tau_{\mathrm{SF}} = 10\,\mathrm{Myr}$, the ratio M/L_K yields an age of 110 Myr.

A.2.2. IRAS 05189-2524

Fig. 12 shows the H-band spectrum integrated across two segments of the NACO slit, located on either side of the nucleus. It shows that even away from the nucleus, the depth of the stellar absorption features is only a few percent. We have therefore decomposed the data into the stellar and non-stellar parts using both the stellar absorption features and the spectral slope of the continuum. The latter method has been shown to work for well sampled data by Davies et al. (2004a). The rationale is that the hot dust associated with the AGN will be much redder than the stellar continuum. An AGN component is also expected to be unresolved for a galaxy at the distance (170 Mpc) of IRAS 05189-2524. The spectral slope was determined by fitting a linear function to the spectrum at each spatial position along the slit. It is plotted as a function of position in Fig. 13, showing a single narrow peak. A Gaussian fit to this yields a spatial resolution of $0.12''$ (100 pc) FWHM. The stellar continuum, also shown in Fig. 13, has been determined by summing the four most prominent absorption features: CO 4-1, Si I, CO 5-2, CO 6-3. While a Gaussian is not an optimal fit to this profile, it does yield an aproximate size scale, which we find to be $0.27''$ FWHM. Quadrature correction with the spatial resolution yields an intrinsic size of $0.25''$ (200 pc). As a cross-check, in the figure we have compared the sum of these two components to the full continuum profile. The good match indicates that the decomposition appears to be reasonable.

Remarkably, the 200 pc size of the nuclear stellar light is very similar to that of the 8.44 GHz radio continuum map of Condon et al. (1991). With a beam size of $0.50'' \times 0.25''$, they resolved the nuclear component to have an intrinsic size of $0.20'' \times 0.17''$. In contrast to radio sources which are powered by AGN and have brightness temperatures $T_{\mathrm{b}} \gg 10^5\,\mathrm{K}$, the emission here is resolved and has a low brightness temperature of $\sim 4000\,\mathrm{K}$. This implies a star forming origin. Using their scaling relations further suggests that the flux density corresponds to a supernova rate of $\sim 1\,\mathrm{yr}^{-1}$.

As described in Section 3, we have estimated the stellar luminosity by comparing the H-band spectrum to a template star to correct for dilution. We used HR 8465 a K 1.5 I star for which the equivalent width of CO 6-3 is 4.2Å, within the 4–5Å range predicted by STARS in Fig. 2. By extrapolating from the spatial profiles along the slit we have estimated the integrated equivalent width within a $1.1''$ aperture, for which Scoville et al. (2000) gave an H-band magnitude of 11.83. Using all four features above we find for the

template $W = 14.4$Å and for IRAS 05189-2524 $W_{CO6-3} = 6.7$Å. This implies that in the central $1.1''$, approximately 45% of the H-band continuum originates in stars. Using the colour conversion $H - K = 0.15$ from Fig. 3 (see Section 3) we find a K-band magnitude for the stars of 12.55 mag and hence a K-band stellar luminosity of $2 \times 10^9 \, L_\odot$. Putting these results together we derive a ratio of supernova rate to K-band stellar luminosity of $\nu_{SN}[yr^{-1}]/L_K[10^{10} L_\odot] \sim 5$. Applying corrections for extinction and an AGN contribution would tend to decrease this ratio.

As a second diagnostic we use $W_{Br\gamma}$. We estimate the dilution of the K-band continuum via two methods. Firstly, we measure $W_{NaI} = 0.3$Å, indicating a stellar fraction of 0.10–0.15. A consistency check is provided by the H-band dilution, which we extrapolate to the K-band using blackbody functions for the stars and dust assuming characteristic temperatures of 5000 K and 1000 K respectively. This method suggests the K-band stellar fraction is around ~ 0.14. Hence correcting the directly measured equivalent width of the narrow Brγ for the non-stellar continuum yields $W_{Br\gamma} = 4$–5Å.

Since IRAS 05189-2524 is close to face-on (Scoville et al. 2000), it is not straightforward to make a reliable estimate of the dynamical mass. Nevertheless, requiring ν_{SN}/L_K to be high while $W_{Br\gamma}$ is low already puts significant constraints on the star formation history. Thus, although the star formation has probably ended, the age is unlikely to be greater than 100 Myr, and could be as low as 50 Myr where ν_{SN}/L_K peaks. For such ages the ratio L_{bol}/L_K is in the range 100–150. Hence for the young stars within $0.55''$ (450 pc) of the nucleus we find $L_{bol} \sim (2$–$3) \times 10^{11} \, L_\odot$, about 20% of L_{bol} for the galaxy.

A.2.3. NGC 2992

The spatial resolution of the K-band data for NGC 2992 has been estimated from both the broad Brγ and the non-stellar continuum (see Section 2 and 3). The two methods yield symmetric PSFs, with FWHMs of $0.32''$ and $0.29''$ respectively, corresponding to 50 pc.

The CO 2-0 equivalent width of ~ 3Å implies a stellar fraction of ~ 0.25 within a radius of $0.4''$, and hence a stellar luminosity of $L_K = 3.5 \times 10^7 \, L_\odot$.

Unlike IRAS 05189-2524, the radio continuum in NGC 2992 is quite complex. Much of the extended emission on scales of a few arcsec appears to originate from a superbubble, driven either by the AGN or by a nuclear starburst. On the other hand, most of the nuclear emission seems to be unresolved. With a beam size of $0.34'' \times 0.49''$, Wehrle & Morris (1988) measured the unresolved flux to be 7 mJy at 5 GHz. At a resolution better than $0.1''$, Sadler et al. (1995) reported a 2.3 GHz flux of 6 mJy. Based on this as well as non-detections at 1.7 GHz and 8.4 GHz, they estimated the core flux at 5 GHz to be <6 mJy. Taking a flat spectral index, as indicated by archival data (Chapman et al. 2000), one might expect the 5 GHz core flux to be not much less than 6 mJy, leaving room for only ~ 1 mJy in extended emission in the central $0.5''$. If we assume this difference can be attributed to star formation, it implies a supernova rate of $\sim 0.003 \, yr^{-1}$ and hence $10^{10} \, \nu_{SN}/L_K \sim 1$. Fig. 4 shows that a ratio of this order is what one might expect for ages up to 200 Myr. However, given the uncertainty it does not impose a significant constraint.

It is also difficult to quantify what fraction of the narrow Brγ is associated with star formation. This is made clear in Fig. 14 which shows that the morphology of the line (centre left panel) does not follow that of the stars (far left). In addition, particularly the south-west side is associated with velocities that are bluer than the surrounding emission, indicative of motion towards us. The western edge also exhibits high velocity dispersion. Taken together, these suggest that we may be seeing outflow from the apex of an ionisation cone

with a relatively large opening angle. This interpretation would tend to support the hypothesis that the radio bubble has been driven by the AGN.

The stellar continuum appears to trace an inclined disk, the north west side of which is more obscured (Fig. 14). However, the velocity dispersion is high, exceeding $150\,\mathrm{km\,s^{-1}}$ across the whole field (Fig. 15). This is similar to the $160\,\mathrm{km\,s^{-1}}$ reported by Nelson & Whittle (1995) from optical spectroscopy, and suggests that we are seeing bulge stars. To analyse the radial luminosity profile we have fitted it with both an $r^{1/4}$ law and exponential profile. The fits in Fig. 16 were optimised at radii $r > 0.5''$ and then extrapolated inwards, convolved with the PSF. Whether one could claim that there is excess continuum in the nucleus depends on the profile fitted. The $r^{1/4}$ law provides a stronger constraint since it is more cuspy, and suggests there is no excess. Although this evidence is inconclusive, Fig. 15 suggests that there is some kinematic evidence favouring the existence of a distinct nuclear stellar population. This comes in the form of a small unresolved drop in dispersion at the centre, similar to those in NGC 1097 and NGC 1068. While the evidence in NGC 2992 is not compelling, the dispersion is consistent with there being an equivalent – but fainter – nuclear disk on a scale of less than our resolution of 50 pc. In general it seems that the K-band light we are seeing is dominated by the bulge, and we are therefore unable to probe in detail the inner region where it seems that more recent star formation has probably occurred.

Thus, although the available data suggest there has likely been recent star formation in the nucleus of NGC 2992, the only strong constraint we can apply is that continuous star formation in the central arcsec over the last Gyr can be ruled out since it would require $W_{\mathrm{Br\gamma}} > 10\text{–}15\text{Å}$. We therefore omit NGC 2992 from the discussion and analysis in Sections 4 and 5.

A.2.4. NGC 1097

In NGC 1097, the first evidence for recent star formation near the nucleus was in the form of a reduction in the stellar velocity dispersion. Emsellem et al. (2001) proposed this could be explained by the presence of a dynamically cold nuclear disk that had recently formed stars. Direct observations of a spiral structure in the central few arcsec, from K-band imaging (Prieto et al. 2005) and [N II] streaming motions (Fathi et al. 2006), have since confirmed this idea. However, some issues remain open, such as why there are three spiral arms rather than the usual two, and why gas along one of them appears to be outflowing.

Our data, at a resolution of $0.25''$ measured from the H-band non-stellar continuum, also reveal the same spiral structure. Indeed, we find that it is traced by the morphology of the CO bandhead absorption as well as by the $2.12\,\mu\mathrm{m}$ H_2 1-0 S(1) line. Interestingly, 1-0 S(1) emission is stronger where the stellar features are weaker. This suggests that obscuration by gas and dust plays an important role. Fig. 18 shows that an $r^{1/4}$ law, typical of stellar bulges, with effective radius $R_{\mathrm{eff}} = 0.5''$ is a good fit to the stellar radial profile at $0.5'' < r < 1.8''$. It therefore seems reasonable to argue that at these radii it is only the gas that lies in a disk. In this picture the spiral structure in the stellar continuum arises solely due to extinction of the stars behind the disk. Extrapolating this fit, convolved with the PSF, to the nucleus indicates that at $r < 0.5''$ there is at least 25% excess stellar continuum. There could be much more, given that it coincides with a change in the dominant kinematics.

For NGC 1097 we parameterized the kinematics of the gas and stars quantitatively using kinemetry. Based on the uniformity of the velocity field, we made the simplifying assumption that across the central $4''$ the gas lies in a single plane whose centre is coincident with the peak of the non-stellar emission. We were then able to derive the position angle and inclination of the disk (see Section 2). The 2D kinematics of the stars

is traced via the CO2-0 absorption bandhead, and that of the gas through the 1-0S(1) emission line. These independently yielded similar parameters: both gave a position angle of $-49°$ and their inclinations were $43°$ and $32°$ respectively. These are fully consistent with values found by other authors (Storchi-Bergmann et al. 2003; Fathi et al. 2006). The resulting rotation curves and velocity dispersions are shown in Fig. 19. The residuals, which can be seen in the velocity field of the gas but not the stars, and their relation to the spiral structure described above will be discussed elsewhere (Davies et al. in prep). The important result here is that at our spatial resolution, we find that the central stellar dispersion is $\sigma_* = 100\,\mathrm{km\,s^{-1}}$, less than the surrounding $150\,\mathrm{km\,s^{-1}}$ and also less than that in the seeing limited spectra of Emsellem et al. (2001). In the same region we find that the rotation velocity of the gas starts to decrease rapidly, and its dispersion increases from $\sigma_{\mathrm{gas}} \sim 40\,\mathrm{km\,s^{-1}}$ to $\sim 80\,\mathrm{km\,s^{-1}}$.

Fig. 19 also shows that while the kinematics of the stars and gas are rather different at large ($> 0.5''$) radii, they are remarkably similar at radii $< 0.5''$. This certainly provides a strong indication that in the nuclear region the stars and gas are coupled, most likely in a (perhaps thick) disk; and that the stars in this disk, which are bright and hence presumably young, give rise to the excess stellar continuum observed.

Evidence for a recent starburst has been found by Storchi-Bergmann et al. (2005) through optical and UV spectra. They argued that a number of features they observed could only arise from an $10^6\,\mathrm{M_\odot}$ instantaneous starburst, which occurred a few Myr ago and is reddened by $A_V = 3\,\mathrm{mag}$ of extinction. Using STARS we have modeled this starburst as a $10^6\,\mathrm{M_\odot}$ burst beginning 8 Myr ago with an exponential decay timescale of 1 Myr. The age we have used is a little older to keep the Brγ equivalent width low; and at this age, the model predicts $W_{\mathrm{Br}\gamma} = 4\text{Å}$. As Fig. 20 shows, the observed Brγ is weak, although perhaps slightly resolved. Corrected for the non-stellar continuum, we measure only $W_{\mathrm{Br}\gamma} \sim 1\text{Å}$. However, the bulge population may account for a significant fraction of the K-band stellar continuum. Correcting also for this could increase $W_{\mathrm{Br}\gamma}$ to 2–5Å, consistent with that of the model – assuming that the Brγ is associated with the starburst rather than the AGN. To within a factor of a few, the scale of the model starburst is also consistent with that measured: In the central $0.5''$ we measure a Brγ flux of $2 \times 10^{-19}\,\mathrm{W\,m^{-2}}$, compared to that predicted by the model of $5 \times 10^{-19}\,\mathrm{W\,m^{-2}}$. Given the uncertainties – factors of a few – both in the parameters of the starburst model and also in the corrections we have applied to the data, we consider this a good agreement.

We cannot constrain the starburst further due to its compactness. Storchi-Bergmann et al. (2005) found that it was occurring in the central $0.2''$, whereas our resolution is only $0.25''$. The Brγ emission is confined to the central 0.4–$0.5''$, although its size is hard to measure due to its weakness with respect to the stellar absorption features. In this region the K-band stellar luminosity is $4.5 \times 10^6\,\mathrm{L_\odot}$. To estimate the dynamical mass we use the mean kinematics of the stars and gas, i.e. $\mathrm{V_{rot}} = 40\,\mathrm{km\,s^{-1}}$ (corrected for inclination) and $\sigma = 90\,\mathrm{km\,s^{-1}}$ (this is the central value, which is least biassed by bulge stars), yielding $1.4 \times 10^8\,\mathrm{M_\odot}$. This is actually dominated by the black hole, which has a mass of $(1.2 \pm 2) \times 10^8\,\mathrm{M_\odot}$ (Lewis & Eracleous 2006). The difference between these implies a mass of gas and stars of $\sim 2 \times 10^7\,\mathrm{M_\odot}$, although with a large uncertainty. The associated mass-to-light ratio is $M/L_K \sim 4$. On its own, this implies that over the relatively large area that it encompasses, the maximum characteristic age for the star formation is a few hundred Myr. If one speculates that star formation has been occurring sporadically for this timescale, then the starburst seen by Storchi-Bergmann et al. (2005) is the most recent active episode.

In order to make a rough estimate of the supernova rate in the central region we make use of measurements reported by Hummel et al. (1987). They find an unresolved component (size $< 0.1''$) with 5 GHz flux density $3.5 \pm 0.3\,\mathrm{mJy}$, but at lower resolution there is a $4.1 \pm 0.3\,\mathrm{mJy}$ component of size $1''$. As discussed in Section 3 we assume that the difference – albeit with only marginal significance – of $0.6 \pm 0.4\,\mathrm{mJy}$ is due to star formation in the central region, which implies a supernova rate of $6 \times 10^{-4}\,\mathrm{yr^{-1}}$ and hence

$10^{10} \nu_{\mathrm{SN}}/L_K \sim 1.3$, a value consistent with rather more recent star formation. Indeed, when compared to Fig. 4, this and the low $W_{\mathrm{Br}\gamma}$ imply a young age and short star formation timescale. For $\tau_{\mathrm{SF}} = 10\,\mathrm{Myr}$ the age is 60–70 Myr; for an instantaneous burst of star formation, the age would be $\sim 10\,\mathrm{Myr}$, broadly consistent with that of Storchi-Bergmann et al. (2005).

Thus, although our data do not uniquely constrain the age of the starburst in the nucleus of NGC 1097, they do indicate that recent star formation has occurred; and they are consistent with a very young compact starburst similar to that derived from optical and UV data.

A.2.5.   NGC 1068

Evidence for a stellar core in NGC 1068 with an intrinsic size scale of $\sim 45\,\mathrm{pc}$ was first presented by Thatte et al. (1997). Based on kinematics measured in large (2–4″) apertures, they assumed the core was virialized and estimated a mass-to-light ratio based on this assumption leading to an upper limit on the stellar age of 1600 Myr. Making a reasonable correction for an assumed old component lead to a younger age of 500 Myr.

Stellar kinematics from optical integral field spectra (Emsellem et al. 2006a; Gerssen et al. 2006) show evidence for a drop in the stellar velocity dispersion in the central few arcsec to $\sigma_* \sim 100\,\mathrm{km\,s^{-1}}$, inside a region of higher 150–200 km s^{-1} dispersion (presumably the bulge). Our near infrared adaptive optics data are able to fully resolve the inner region where σ_* drops, as shown in Fig. 21. As for NGC 1097, the velocity distribution of the stars was derived through kinemetry, again making use of the uniformity of the stellar velocity field to justify the simplifying assumption that the position angle and inclination do not change significantly in the central 4″. The derived inclination of 40° and position angle of 85° are quantitatively similar to those found by other authors in the central few to tens of arcseconds (Emsellem et al. 2006a; Gerssen et al. 2006; García-Lorenzo et al. 1999). The uniformity of the stellar kinematics is in contrast to molecular gas kinematics, as traced via the 1-0 S(1) line, which are strongly perturbed and show several distinct structures superimposed. These are too complex to permit a comparably simple analysis and will be discussed, together with the residuals in the stellar kinematics in a future work (Mueller Sánchez et al. in prep).

The crucial result relevant here is that at our H-band resolution of 0.10″ we find that σ_* reduces from 130 km s^{-1} at 1–2″ to only 70 km s^{-1} in the very centre. That there is in the same region an excess in the stellar continuum is demonstrated in Fig. 22. Here we show the radial profile of the stellar continuum from both SINFONI integral field spectra out to a radius of 2″ and NACO longslit spectra out to 5″ (350 pc). At radii 1–5″, corresponding roughly to the region of high stellar dispersion measured by Emsellem et al. (2006a), the profile is well matched by an $r^{1/4}$ law, as one might expect for a bulge. At radii $r < 1″$ – the same radius at which we begin to see a discernable reduction in the stellar dispersion – the stellar continuum increases by as much as a factor 2 above the inward extrapolation of the profile, indicating that there is extra emission. As for NGC 1097, the combined signature of dynamically cool kinematics and excess emission is strong evidence for a nuclear disk which has experienced recent star formation.

We can make an estimate of the characteristic age of the star formation in the central arcsec based on the mass-to-light ratio in a similar way to Thatte et al. (1997). Because the stars appear to lie in a disk, we estimate the dynamical mass as described in Section 3 from the stellar kinematics, using the rotation velocity and applying a correction for the dispersion. The stellar rotation curve is essentially flat at 0.1–0.5″, with $V_* = 45\,\mathrm{km\,s^{-1}}$ (corrected for inclination). We also take $\sigma_* = 70\,\mathrm{km\,s^{-1}}$, which is the central value and

hence least biassed by the high dispersion bulge stars. These lead to a mass of $1.3 \times 10^8\,\mathrm{M}_\odot$ within $r = 0.5''$ (35 pc), and a mean surface density of $3 \times 10^4\,\mathrm{M}_\odot\,\mathrm{pc}^{-2}$. Correcting for the non-stellar continuum, the H-band magnitude (which the behaviour of σ_* indicates is dominated by the disk emission) in the same region is 11.53 mag. For $H - K = 0.15$ mag (Fig. 4), we find $L_K = 4.3 \times 10^7\,\mathrm{L}_\odot$ and hence $M/L_K = 3\,\mathrm{M}_\odot/\mathrm{L}_\odot$. If no star formation is on-going, this implies a characteristic age of 200–300 Myr fairly independent of the timescale (for $\tau_{\mathrm{SF}} \lesssim 100\,\mathrm{Myr}$, see Fig. 4) on which stars were formed. We note that this is significantly younger than the age estimated by Thatte et al. (1997) primarily because their mass was derived using a higher σ_* corresponding to the bulge stars.

The assumption of no current star formation is clearly demonstrated by the Brγ map in Fig. 23. Away from the knots of Brγ, which are associated with the coronal lines and the jet rather than possible star formation, the equivalent width is $W_{\mathrm{Br}\gamma} \sim 4$Å. This is significantly less than that for continuous star formation of any age. Thus, while it seems likely that star formation has occurred in the last few hundred Myr, it also seems an unavoidable conclusion that there is no current star formation.

To complete our set of diagnostics for NGC 1068, we consider also the radio continuum. This is clearly dominated by phenomena associated with the AGN and jets, and our best estimate of the flux density away from these features is given by the lowest contour in maps such as Figure 1 of Gallimore et al. (2004). From this we estimate an upper limit to the 5 GHz continuum associated with star formation of 128 mJy within $r < 0.5''$. However, converting to a supernova rate and comparing to the K-band stellar luminosity yields a limit that is not useful, being an order of magnitude above the largest expected values.

A.2.6. NGC 3783

At near infrared wavelengths, the AGN in NGC 3783 is remarkably bright. Integrated over the central $0.5''$ less than 4% of the K-band continuum is stellar. In addition, the broad Brackett lines are very strong and dominate the H-band. Both of these phenomena are immediately clear from the H- and K-band spectra in Fig. 24. However, it does mean that the spatial resolution can be measured easily from both the non-stellar continuum and the broad emission lines (see Section 2). We find the K-band PSF to be symmetrical with a FWHM of $0.17''$.

Due to the ubiquitous Brackett emission in the H-band we were unable to reliably trace the stellar absorption features and map out the stellar continuum. Instead we have used the CO 2-0 bandhead at 2.3μm even though the dilution at the nucleus itself is extreme. The azimuthally averaged radial profile is shown in Fig. 25 together with the PSF for reference. At radii from $0.2''$–$1.6''$ (the maximum we can measure) the profile is well fit by an $r^{1/4}$ de Vaucouleurs law with $R_{\mathrm{eff}} = 0.6''$ (120 pc). As has been the case previously, at smaller radii we find an excess that here is perhaps marginally resolved. Thus a substantial fraction of the near infrared stellar continuum in the central region is likely to originate in a population of stars distinct from the bulge.

We were unable to measure the stellar kinematics due to the limited signal-to-noise. Instead, we used the molecular gas kinematics to estimate the dynamical mass. As before, we used kinemetry to derive the position angle of $-14°$ and the inclination in the range 35–39°. This orientation is consistent with the larger ($20''$) scale isophotes in the J-band 2MASS image and implies that in NGC 3783 there is no significant warp on scales of 50 pc to 4 kpc. A small inclination is also consistent with its classification as a Seyfert 1. Adopting these values, the resulting rotation curve is shown in Fig. 26. At very small radii the rising rotation curve may be the result of beam smearing across the nucleus. At $r > 0.2''$, the falling curve suggests that

the rotation is dominated by the central ($r < 0.2''$) mass, perhaps the supermassive black hole. We estimate the dynamical mass within a radius of $0.3''$ (60 pc), corresponding to the point where the excess continuum begins and also where the rotation curve appears to be unaffected by beam smearing.

Taking $V_{\rm rot} = 60\,{\rm km\,s^{-1}}$ and $\sigma = 35\,{\rm km\,s^{-1}}$ we derive a dynamical mass of $M_{\rm dyn} = 1.0 \times 10^8\,{\rm M_\odot}$. The black hole mass of $3 \times 10^7\,{\rm M_\odot}$ (from reverberation mapping, Peterson et al. 2004) is only 30% of this, and so cannot be dominating the dynamics on this scale unless its mass is underestimated. With respect to this, we note that Peterson et al. (2004) claim the statistical uncertainty in masses derived from reverberation mapping is about a factor 3. Alternatively, there may be a compact mass of gas and stars at $r < 0.3''$. However, including σ in the mass estimate implicitly assumes that the dispersion arises from macroscopic motions. On the other hand, because we are observing only the hot H_2, it is possible that the dispersion is dominated by turbulence arising from shocks or UV heating of clouds that generate the 1-0 S(1) emission – issues that are discussed in more detail by Hicks et al. (in prep.). In this case we will have overestimated the dynamical mass. Excluding σ from the mass estimation yields $M_{\rm dyn} = 5 \times 10^7\,{\rm M_\odot}$. We consider these two estimates as denoting the maximum range of possible masses. Subtracting $M_{\rm BH}$ then gives a mass of stars and gas in the range $(2\text{–}7)\times10^7\,{\rm M_\odot}$, implying a mass surface density of $1700\text{–}6000\,{\rm M_\odot\,pc^{-2}}$ and $M/L_K = 0.6\text{–}2.1\,{\rm M_\odot/L_\odot}$. Based on these ratios alone, Fig 4 indicates that the characteristic age of the star formation may be as low as $\sim 70\,{\rm Myr}$, although it could also be an order of magnitude greater. Without additional diagnostics we cannot discriminate further.

We are unable to use Brγ as an additional constraint on the star formation history. Its morphology and velocity field are similar to that of [SiVI], and rather different from the 1-0 S(1). It shows an extension to the north which appears to be outflowing at $> 50\,{\rm km\,s^{-1}}$ (Fig 27) – perhaps tracing an ionisation cone. Since the Brγ resembles the [SiVI], it is reasonable to conclude that it too is associated with the AGN rather than star formation. Thus the equivalent width of Brγ (with respect to the stellar continuum) of $W_{\rm Br\gamma} = 30\text{\AA}$ represents an upper limit to that associated with star formation.

The radio continuum in the nucleus of NGC 3783 has been measured with several beam sizes at 8.5 GHz. For a beam of $1.59'' \times 0.74''$, Morganti et al. (1999) found it was unresolved with a flux density of $8.15 \pm 0.24\,{\rm mJy}$. With a smaller $\sim 0.25''$ beam, Schmitt et al. (2001) measured a total flux density of 8.0 mJy dominated by an unresolved component of $7.7 \pm 0.05\,{\rm mJy}$. At smaller scales still of $\sim 0.03''$ corresponding to 6 pc, Sadler et al. (1995) placed an upper limit on the 8.5 GHz flux density of 7 mJy. Taken together, these results imply that there is some modest 8.5 GHz radio continuum of 0.7–1 mJy extended on scales of $0.3\text{–}1''$. Based on this we estimate a supernova rate as described in Section 3 of $\sim 0.007\,{\rm yr^{-1}}$, and hence a ratio $10^{10}\,\nu_{\rm SN}/L_K \sim 2$. Given that the unresolved radio continuum on the smallest scales is an upper limit, the extended component may be stronger and hence the true $\nu_{\rm SN}/L_K$ ratio may be greater than that estimated here. Fig 4 then puts a relatively strong limit of $\sim 50\,{\rm Myr}$ on the maximum age of the star formation.

This age is fully consistent with that above associated with our lower mass estimate. The value of $W_{\rm Br\gamma} < 30\text{\AA}$ above does not impose additional constraints, although we note that if the Brγ flux associated with star formation is only a small fraction of the total then it would imply that the timescale over which the star formation was active is no longer than a few times $\sim 10\,{\rm Myr}$. Therefore in the nucleus ($r < 0.3''$) of NGC 3783 we adopt 50–70 Myr as the age of the star formation and $M_{\rm dyn} = 2 \times 10^7\,{\rm M_\odot}$ as the dynamical mass excluding the central supermassive black hole.

REFERENCES

Abuter R., Schreiber J., Eisenhauer F., Ott T., Horrobin M., Gillesen S., 2006, NewAR, 50, 398

Anantharamaiah K., Viallefond F., Mohan R., Goss W., Zhao J., 2000, ApJ, 537, 613

Asari N., Vega L., Garcia-Rissmann A., González Delgado R., Storchi-Bergmann T., Cid Fernandes R., 2007, in *Galaxy Evolution Across the Hubble Time*, eds Combes F., Palous J., IAU Symposium 235, 71

Baganoff F., et al., 2003, ApJ, 591, 891

Balcells M., Graham A., Domínguez-Palmero L., Peletier R., 2003, ApJ, 582, L79

Bender R., Burstein D., Faber S., 1992, ApJ, 399, 462

Bland-Hawthorne J., Lumsden S., Voit G., Cecil G., Weisheit J., 1997, Ap&SS, 248, 177

Bondi H., 1952, MNRAS, 112, 195

Bonnet H., et al., 2004, The ESO Messenger, 117, 17

Brand K., et al., 2006, ApJ, 663, 204

Capetti A., Axon D., Macchetto F., Marconi A., Winge C., 1999, ApJ, 516, 187

Carilli C., Wrobel J., Ulvestad J., 1998, AJ, 115, 928

Chapman S., Morris S., Alonso-Herrero A., Falcke H., 2000, MNRAS, 314, 263

Chevalier R., 1977, ARA&A, 15, 175

Chevalier R., Fransson C., 2001, ApJ, 558, L27

Cid Fernandes R., Gu Q., Melnick J., Terlevich E., Terlevich R., Kunth D., Rodrigues Lacerda R., Joguet B., 2004, MNRAS, 355, 273

Cid Fernandes R., Heckman T., Schmitt H., González Delgado R., Storchi-Bergmann T., 2001, ApJ, 558, 81

Colina L., Alberdi A., Torrelles J., Panagia N., Wilson A., 2001, ApJ, 553, L19

Condon J., Huang Z.-P., Yin Q., Thuan T., 1991, ApJ, 378, 65

Condon J., 1992, ARA&A, 30, 575

Côté P., et al., 2006, ApJS, 165, 57

Cuadra J., Nayakshin S., Springel V., Di Matteo T., 2006, MNRAS, 366, 358

Dasyra K., et al., 2006, ApJ, 651, 835

Davies R., Sternberg A., Lehnert M., Tacconi-Garman L., 2003, ApJ, 597, 907

Davies R., Tacconi L., Genzel R., 2004a, ApJ, 602, 148

Davies R., Tacconi L., Genzel R., 2004b, ApJ, 613, 781

Davies R., Sternberg A., Lehnert M., Tacconi-Garman L., 2005, ApJ, 633, 105

Davies R., et al., 2006, ApJ, 646, 754

Davies R., 2007a, MNRAS, 375, 1099

Davies R., 2007b in *The 2007 ESO Instrument Calibration Workshop*, ESO Astrophysics Symposia, arXiv:astro-ph/0703044

Downes D., Solomon P., 1998, ApJ, 507, 615

Eisenhauer F., et al., 2003, in *Instrument Design and Performance for Optical/Infrared Ground-based Telescopes*, eds. Masanori I., Moorwood A., Proc. SPIE, 4841, 1548

Emsellem E., Greusard D., Combes F., Friedli D., Leon S., Pécontal E., Wozniak H., 2001, A&A, 368, 52

Emsellem E., Fathi K., Wozniak H., Ferruit P., Mundell C., Schinnerer E., 2006a, MNRAS, 365, 367

Emsellem E., 2006b, in *The Central Engine of Active Galactic Nuclei*, eds Ho L., Wang J.-M. (San Francisco: ASP)

Emsellem E., 2006c, in *Mapping the Galaxy and Nearby Galaxies*, eds Wada K., Combes F. (Springer)

Fathi K., Storchi-Bergmann T., Riffel R., Winge C., Axon D., Robinson A., Apetti A., Marconi A., 2006, ApJ, 641, L25

Förster Schreiber N., Genzel R., Lutz D., Sternberg A., 2003, ApJ, 599, 193

Förster Schreiber N., 2000, AJ, 120, 2089

Gallimore J., Baum S., O'Dea C., 2004, ApJ, 613, 794

García-Lorenzo B., Mediavilla E., Arribas S., 1999, ApJ, 518, 190

Genzel R., Weitzel L., Tacconi-Garman L.E., Blietz M., Cameron M., Krabbe A., Lutz D., Sternberg A., 1995, ApJ, 444, 129

Genzel R., et al., 2003, ApJ, 594, 812

Gerssen J., Allington-Smith J., Miller B., Turner J., Walker A., 2006, MNRAS, 365, 29

Glass I., 1984, MNRAS, 211, 461

González Delgado R., Heckman T., Leitherer C., 2001, ApJ, 546, 845

González Delgado R., Cid Fernandes R., 2005, in *Starbursts: from 30 Doradus to Lyman Break Galaxies*, eds de Grijs R., González Delgado R., (Dordrecht: Springer), ASSL, 329, 263

Graham A., Guzmán R., 2003, AJ, 125, 2936

Granato G., de Zotti G., Silva L., Bressan A., Danese L., 2004, ApJ, 600, 580

Greenhill L., et al., 2003, ApJ, 590, 162

Gu Q., Dultzin-Hacyan D., de Diego J., 2001, RMxAA, 37, 3

Heckman T., González-Delgado R., Leitherer C., Meurer G., Krolik J., Wilson A., Koratkar A., Kinney A., 1997, ApJ, 482, 114

Huang Z., Thuan T., Chevalier R., 1994, ApJ, 424, 114

Hummel E., van der Hulst J., Keel W., 1987, A&A, 172, 32

Ivanov V., Rieke G., Groppi C., Alonso-Herrero A., Rieke M., Engelbracht C., 2000, ApJ, 545, 190

Johuet B., Kunth D., Melnick J., Terlevich R., Terlevich E., 2001, A&A, 380, 19

Kennicutt Jr R., 1998, ApJ, 498, 541

Knapen J., 2004, in *Penetrating bars through masks of cosmic dust : the Hubble tuning fork strikes a new note*, eds Block D., Puerari I., Freeman K., Groess R., Block E. (Dordrecht: Kluwer Academic Publishers), ASSL, vol. 319, p.189

Kormendy J., Sanders D., 1992, ApJ, 390, L53

Kormendy J., Fisher D., Cornell M., Bender R., 2007, ApJ, submitted

Krajnović D., Cappellari M., de Zeeuw T., Copin Y., 2006, MNRAS, 366, 787

Krolik J., 2007, ApJ, in press

Krumholz M., McKee C., Klein R., 2006, ApJ, 638, 369

Leitherer C., et al., 1999, ApJS, 123, 3

Lenzen R., et al., 2003, in *Instrument Design and Performance for Optical/Infrared Ground-based Telescopes*, eds. Masanori I., Moorwood A., Proc. SPIE, 4841, 944

Lewis K., Eracleous M., 2006, ApJ, 642, 711

Lodato G., Bertin G., 2003, A&A, 398, 517

Lonsdale C., Smith H., Lonsdale C., 1995, ApJ, 438, 632

Machalski J., Chyży K., Stawarz Ł., KoziełD., 2007, A&A, 462, 43

Maiolino R., Krabbe A., Thatte N., Genzel R., 1998, ApJ, 493, 650

Martinez-Sansigre A., Rawlings S., Lacy M., Fadda D., Jarvis M., Marleau F., Simpson C., Willott C., 2006, MNRAS, 370, 1479

Martini P., Regan M., Mulchaey J., Pogge R., 2003, ApJ, 589, 774

Márquez I., Masegosa J., Durret F., González Delgado R., Moles M., Maza J., Pérez E., Roth M., 2003, A&A, 409, 459

Melia F., ApJ, 387, L25

Mihos C., Hernquist L., 1994, ApJ, 437, L47

Morganti R., Tsvetanov Z., Gallimore J., Allen M., 1999, A&AS, 137, 457

Mueller Sánchez F., Davies R., Eisenhauer F., Tacconi L., Genzel R., Sternberg A., 2006, A&A, 454, 481

Nelson C., Whittle M., 1995, ApJS, 99, 67

Nikolaev S., Weinberg M., 1997, ApJ, 487, 885

Oliva E., Origlia L., Kotilainen J., Moorwood A., 1995, A&A, 301, 55

Origlia L., Moorwood A., Oliva E., 2003, A&A, 280, 536

Ozernoy L, Genzel R., 1996, eds Blitz L., Teuben P., (Kluwer) Proc. IAU Symposium 169, p.181

Ozernoy L., Genzel R., Usov V., 1997, MNRAS, 288, 1997

Paumard T., Maillard J.-P., Morris M., Rigaut F., 2001, A&A, 366, 466

Paumard T., et al., 2006, ApJ, 643, 1011

Peterson B., et al., 2004, ApJ, 613, 682

Pier E., Krolik J., 1992, ApJ, 399, L23

Pier E., Antonucci R., Hurt T., Kriss G., Krolik J., 1994, ApJ, 428, 124

Prieto A., Maciejewski W., Reunanen J., 2005, AJ, 130, 1472

Rigby J., Rieke G., Donley J., Alonso-Herrero A., Pérez-González P., 2006, ApJ, 645, 115

Rousset G., et al., 2003, in *Adaptive Optical System Technologies II*, eds. Wizinowich P., Bonaccini D., Proc. SPIE, 4839, 140

Sadler E., Slee O., Reynolds J., Roy A., 1995, MNRAS, 276, 1273

Sarzi M., Shields J., Pogge R., Martini P., 2007, in *Stellar Populations as Building Blocks of Galaxies*, eds Peletier R., Vazdekis A., IAU Symposium 241

Schmitt H., Ulvestad J., Antonuccci R., Kinney A., 2001, ApJS, 132, 199

Scoville N., et al., 2000, AJ, 119, 991

Scoville N., 2003, JKAS, 36, 167

Shapiro K., Gerssen J., van der Marel R., 2003, AJ, 126, 2707

Smith H., Lonsdale C., Lonsdale C., Diamond P., 1998, ApJ, 493, L17

Springel V., Di Matteo T., Hernquist L., 2005, MNRAS, 361, 776

Sternberg A., 1998, ApJ, 506, 721

Sternberg A., Hoffman T., Pauldrach A., 2003, ApJ, 599, 1333

Storchi-Bergmann T., González Delgado R., Schmitt H., Cid Fernandes R., Heckman T., 2001, ApJ, 559, 147

Storchi-Bergmann T., et al., 2003 ApJ, 598, 956

Storchi-Bergamnn T., Nemmen R., Spinelli P., Eracleous M., Wilson A., Filippenko A., Livio M., 2005, ApJ, 624, L13

Thatte N., Quirrenbach A., Genzel R., Maiolino R., Tecza M., 1997, ApJ, 490, 238

Thompson T., Quataert E., Murray N., 2005, ApJ, 630, 167

Vazquez G., Leitherer C., 2005, ApJ, 621, 695

Wehrle A., Morris M., 1988, AJ, 95, 1689

Winters J., Le Bertre T., Jeong K., Nyman L.-Å., Epchtein N., 2003, A&A, 409, 715

Woo J.-H., Urry C., 2002, ApJ, 579, 530

Wozniak H., Combes F., Emsellem E., Friedli D., 2003, A&A, 409, 469

Table 1.   Table of Observations

Object	Band[a]	Res.[b] ($''$)	Date	Instrument
Mkn 231[c]	H	0.176	May '02	Keck, NIRC2
NGC 7469[c]	K	0.085	Nov '02	Keck, NIRSPAO
	K	0.15	Jul '04	VLT, SINFONI
Circinus[c]	K	0.22	Jul '04	VLT, SINFONI
NGC 3227[c]	K	0.085	Dec '04	VLT, SINFONI
IRAS 05189-2524	H	0.12	Dec '02	VLT, NACO
NGC 2992	K	0.30	Mar '05	VLT, SINFONI
NGC 1097	H	0.245	Oct '05	VLT, SINFONI
NGC 1068	H	0.10	Oct '05	VLT, SINFONI
	H	0.13	Dec '02	VLT, NACO
NGC 3783	K	0.17	Mar '05	VLT, SINFONI

[a]Band used for determining the quantitative star formation properties. NGC 1097, NGC 1068, and NGC 3783 were actually observed in H and K bands.

[b]Spatial resolution (FWHM) estimated from the data itself, using the methods described in Section 2.

[c]References to detailed studies of individual objects: Mkn 231 (Davies et al. 2004b), NGC 7469 (Davies et al. 2004a), Circinus, (Mueller Sánchez et al. 2006), NGC 3227 (Davies et al. 2006).

Table 2.   Summary of basic data for AGN

Object	Classification[a]	Distance Mpc	$\log\frac{L_{\mathrm{bol}}}{L_\odot}$ [b]	$\log\frac{M_{\mathrm{BH}}}{M_\odot}$	Ref.[c] for M_{BH}
Mkn 231	ULIRG, Sy 1, QSO	170	12.5	7.2	1
NGC 7469	Sy 1	66	11.5	7.0	2
Circinus	Sy 2	4	10.2	6.2	3
NGC 3227	Sy 1	17	10.2	7.3	4
IRAS 05189-2524	ULIRG, Sy 1	170	12.1	7.5	1
NGC 2992	Sy 1	33	10.7	7.7	5
NGC 1097	LINER, Sy 1	18	10.9	8.1	6
NGC 1068	Sy 2	14	11.5	6.9	7
NGC 3783	Sy 1	42	10.8	7.5	2

[a] Classifications are taken primarily from the NASA/IPAC Extragalactic Database. In addition, we have labelled as Seyfert 1 those for which we have observed broad (i.e. FWHM $> 1000\,\mathrm{km\,s^{-1}}$) Br$\gamma$; see also Fig 1.

[b] Calculated in the range 8–1000 μm from the IRAS 12–100 μm flux densities; with an additional correction for optical and near-infrared luminosity in cases where appropriate.

[c] References for black hole masses: (1) Dasyra et al. (2006); (2) Peterson et al. (2004); (3) Greenhill et al. (2003); (4) Davies et al. (2006); (5) Woo & Urry (2002); (6) Lewis & Eracleous (2006); (7) Lodato & Bertin (2003)

Table 3.   Measured & Derived Properties of the Nuclei[a]

Object	radius		$\log\frac{L_{K}*}{L_{\odot}}$	$\log\frac{M_{\mathrm{dyn}}}{M_{\odot}}$	Σ_{dyn}	$W_{\mathrm{Br}\gamma}$	M_{dyn}/L_K	$10^{10}\nu_{SN}/L_K$	age	$\langle\mathrm{SFR}\rangle$
	$''$	pc			$10^4\,M_{\odot}\,pc^{-2}$	Å	$M_{\odot}/L_{\odot}$	$\mathrm{yr}^{-1}\,L_{\odot}^{-1}$	Myr	$M_{\odot}\,\mathrm{yr}^{-1}\,\mathrm{kpc}^{-2}$
Mkn 231[b]	0.6	480	9.3	9.8	0.9	—	3.1	20	120–250	25–50
NGC 7469	0.4	128	8.5	8.7	1.0	11	1.6	3	110–190	50–100
Circinus	0.4	8	6.2	7.5	17	30	23	1.5	80	~70
NGC 3227[c]	0.4	32	7.8	8.0	3.7	4	1.9	2.2	40	~380
IRAS 05189-2524	0.55	450	9.3	—	—	4	—	5	50–100	30–70
NGC 2992[d]	0.4	64	7.5	—	—	<12	—	1	—	—
NGC 1097[e]	0.25	22	6.7	8.2	1.3	1	4.5	1.4	8	~80
NGC 1068	0.5	35	7.6	8.1	3.4	4	3.0	<20	200–300	90–170
NGC 3783[f]	0.3	60	7.5	7.3	0.2	<30	0.6	2	50–70	30–60

[a] The methods used to measure these quantities (within the radii given) are described in Section 3. Specific issues associated with individual objects are discussed in Appendix A.

[b] M_{dyn} depends strongly on even small changes to the inclination; here it is given for $i = 10°$. Correcting M_{dyn} for an estimate of the gas mass given in Downes & Solomon (1998) yields $M/L_K = 2.3 M_{\odot}/L_{\odot}$.

[c] The best star formation models indicate that M/L_K is much less than the limit given here using the dynamical mass.

[d] It is likely that much of the narrow Brγ in the nuclear region here is associated with an ionisation cone. In addition, the high stellar velocity dispersion, even on the smallest scales we have been able to measure, suggests that the K-band light is dominated by the bulge.

[e] Correcting $W_{\mathrm{Br}\gamma}$ for the old stellar population would probably yield a value in the range 2–5Å. Even on this scale the dynamical mass is dominated by the supermassive black hole. Both Σ_{dyn} and M/L_K are estimated after subtracting M_{BH}.

[f] Much of the Brγ here is outflowing and hence associated with the AGN. M_{dyn} is derived from gas kinematics as described in the text. Both Σ_{dyn} and M/L_K are estimated after subtracting M_{BH}.
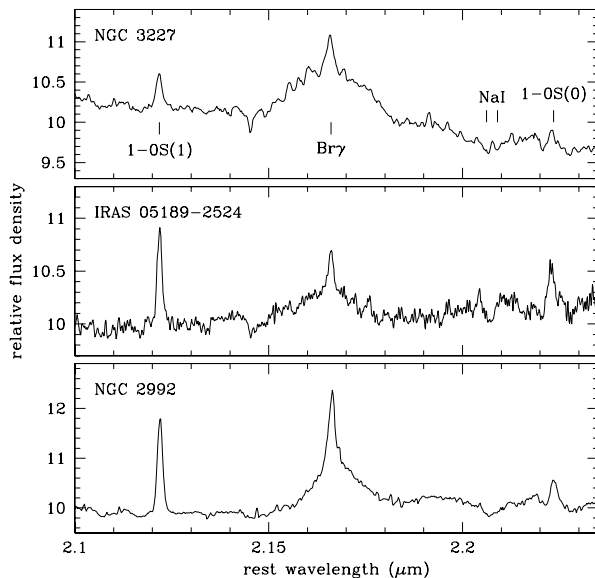
Fig. 1.— K-band spectra showing broad Brγ emission in 3 AGN which are not usually classified as Seyfert 1. Top: NGC 3227 (0.25″ aperture); Middle: IRAS 05189−2524 (1″ aperture); Bottom: NGC 2992 (0.5″ aperture). The most prominent emission and absorption features are marked.
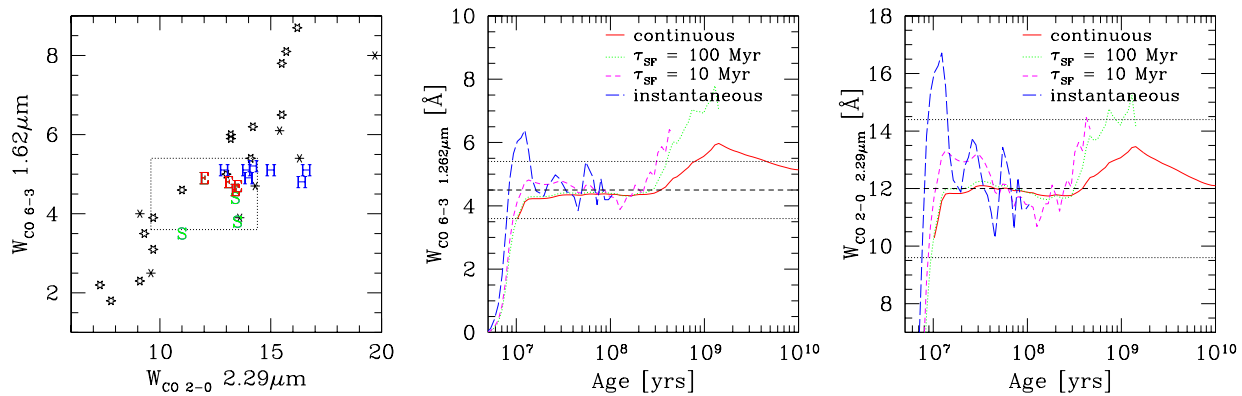
Fig. 2.— Left: equivalent width of the CO 2-0 and CO 6-3 features for various stars and galaxies. The late-type supergiant stars (skeletal star shapes) and giant stars (open star shapes) are taken from Origlia et al. (1993). The galaxies (denoted 'E' for elliptical, 'S' for spiral, and 'H' for star forming HII galaxy) are from Oliva et al. (1995). The dashed box encloses the region for which there is no more than 20% deviation from each of the values $W_{CO2-0} = 12$Å and $W_{CO6-3} = 4.5$Å. Centre and right: calculated W_{CO6-3} and W_{CO2-0} respectively from STARS for several different star formation histories. Each line is truncated when the cluster luminosity falls below 1/15 of its maximum. In each case, the dashed lines show typical values adopted, and the dotted lines denote a range of ±20%.
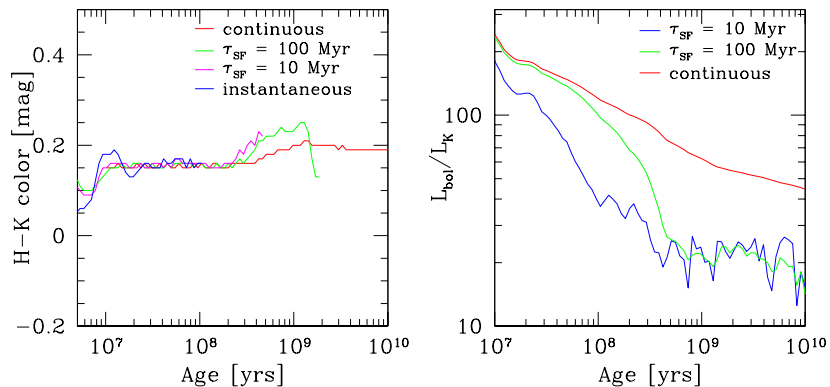
Fig. 3.— Left: H-K colour of star clusters with different star formation timescales and ages, as calculated by STARS. Right: Ratio of bolometric to K-band luminosity. Although the range of 20–200 initially appears large, the uncertainty on an intermediate value of 60 is only 0.3 dex. This is small compared to the range of interest in the paper, which is several orders of magnitude.
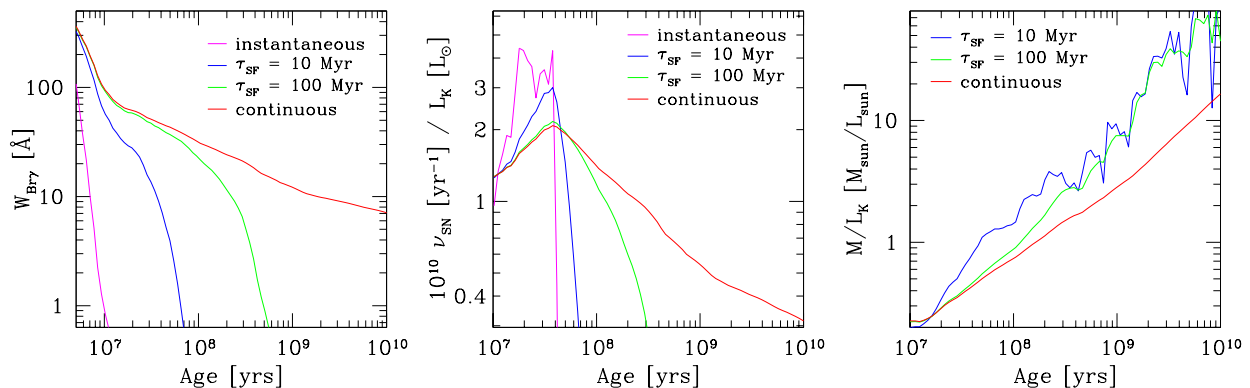
Fig. 4.— Various diagnostics calcuated with STARS for several star formation timescales, as functions of age: Brγ equivalent width, supernova rate, and mass-to-light ratio. Note that all are normalised to the K-band stellar continuum; and that L_K is the total luminosity in the 1.9–2.5μm band in units of bolometric solar luminosity ($1\,L_{\rm bol} = 3.8 \times 10^{26}\,W$), rather than the other frequently used monochromatic definition which has units of the solar K-band luminosity density.
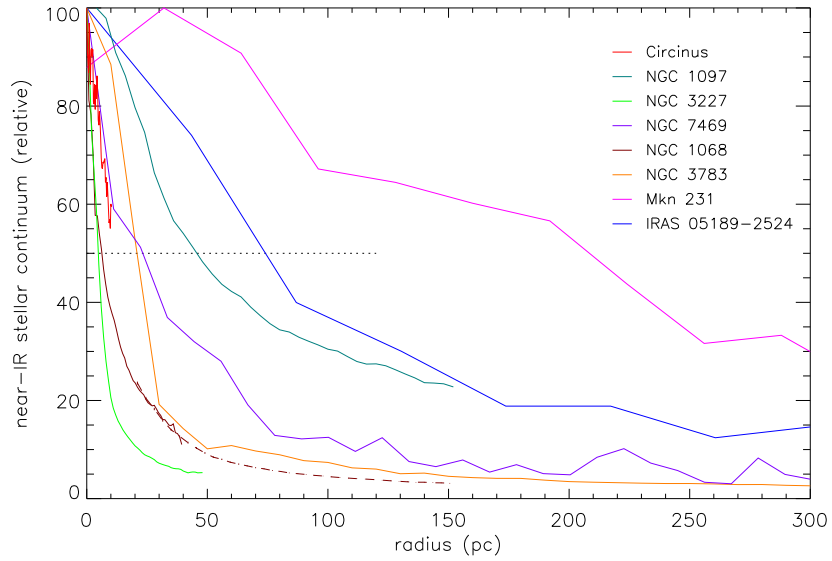
Fig. 5.— Size scales of nuclear star forming regions. The profile has been determined from the CO absorption features in the H or K band, which are approximately independent of star formation history (see text for details). For longslit data, spatial profiles have been averaged; for integral field data, azimuthally averaged proifles are shown. For NGC1068, data at two different pixel scales are shown (corresponding to the solid and dashed brown lines). The horizontal dotted line is drawn at half-maximum height, to assist in estimating size scales by eye.
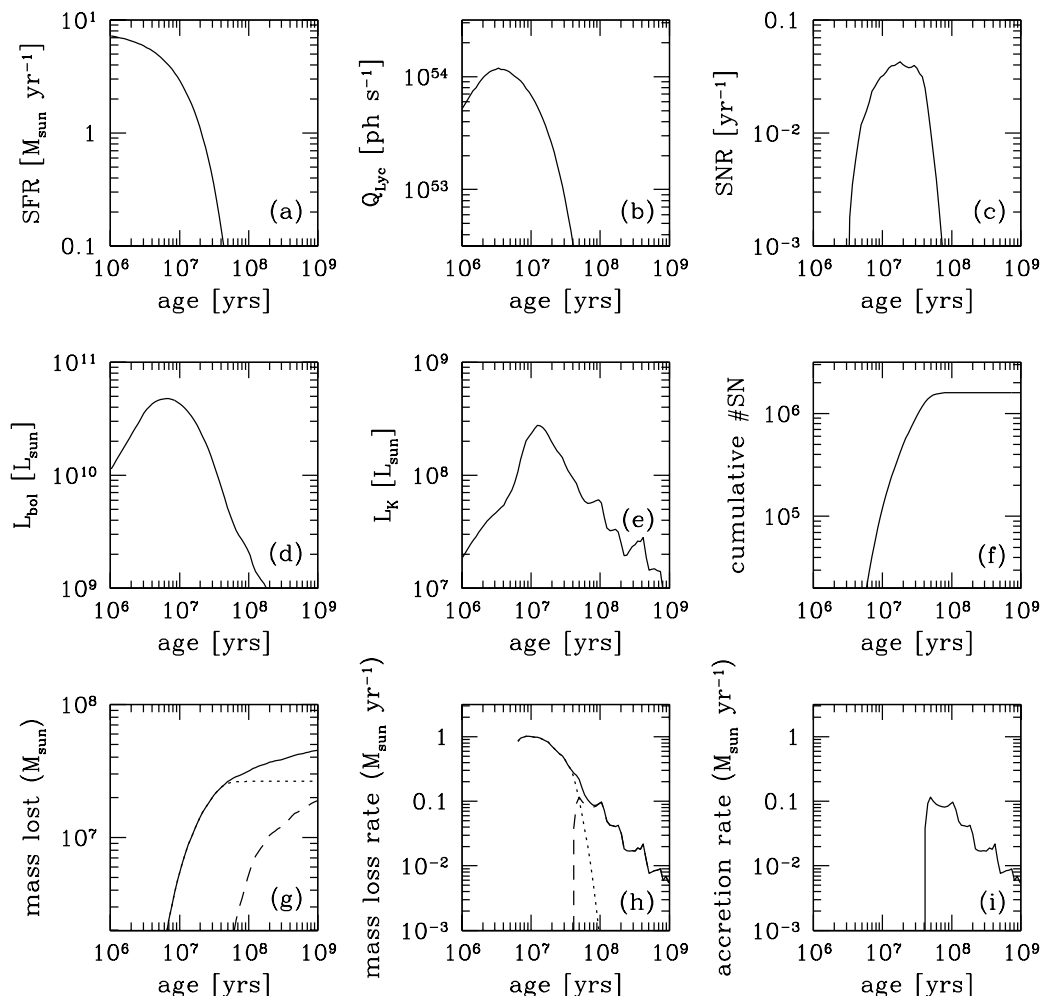
Fig. 6.— A STARS star formation model based on the main characteristics of the observed starbursts, which is illustrative of a 'typical' nuclear starburst that we have observed. The scaling is fixed as $2 \times 10^9 \, \mathrm{M_\odot}$ (typical of that within a $30 \, \mathrm{pc}$ radius; Fig. 9) at an age of $100 \, \mathrm{Myr}$ (the typical age in Table 3). The star formation timescale is $\tau_{\mathrm{SF}} = 10 \, \mathrm{Myr}$ to reproduce a low Brγ equivalent width. The panels are, from top left: (a) star formation rate (SFR); (b) number of ionising photons (Q_{Lyc}, proportional to the Brγ luminosity); (c) supernova rate (SNR); (d) bolometric luminosity (L_{bol}); (e) K-band luminosity (L_K); (f) cumulative number of supernovae; (g) cumulative mass that has been recycled back into the ISM by supernovae and winds; (h) mass loss rate from stars; (i) rate at which the lost mass can in principle be accreted onto a central supermassive black hole (due to its outflow speed; see text for details). In the last two panels, the mass loss is split into that due to OB and Wolf-Rayet stars and supernovae (dotted lines), and that due to late-type and AGB stars (dashed lines). Stellar mass loss in STARS is accounted for at the end of each star's life as the difference in mass between the original (ZAMS) stellar mass and the remnant mass as the end-product of its stellar evolution, as described in Sternberg (1998). For this reason, the mass loss rates from OB and Wolf-Rayet stars do not appear explicitly in panel (h) at very young cluster ages.
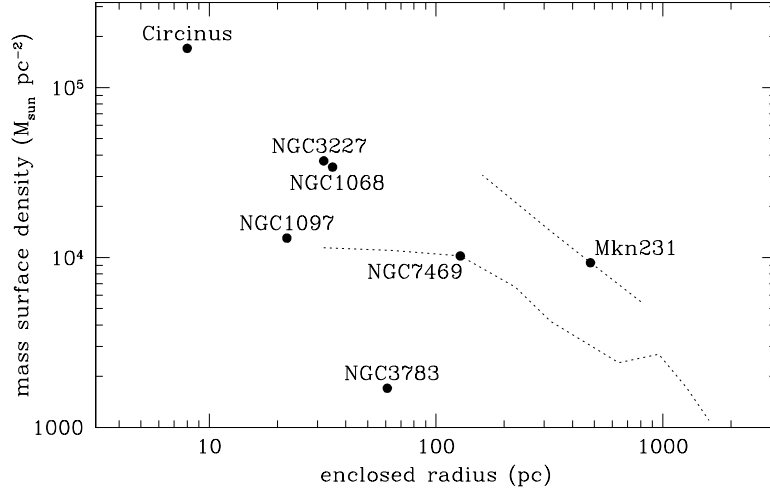
Fig. 7.— Mean enclosed mass surface density as a function of radius. The points are from data given in Table 3; the dashed lines represent the mass models derived for NGC 7469 and Mkn 231 (Davies et al. 2004a,b). The galaxies all follow the same trend towards increasing densities in the central regions.
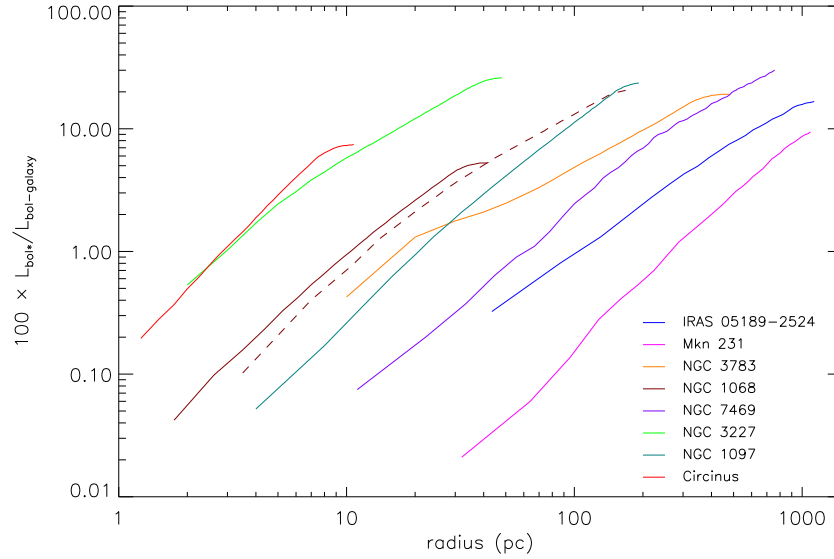
Fig. 8.— Integrated bolometric luminosity of the young stars L_{bol*} as a fraction of that of the galaxy $L_{bol-galaxy}$, plotted as a function of radius. L_{bol*} is calculated from the stellar L_K or L_H assuming that, on the generally small scales here, all the near infrared stellar continuum originates in the young stars. On 10 pc scales the contribution of young stars is at most a few percent of the galaxy's total luminosity, while on kpc scales it may be significant and hence comparable to the AGN luminosity. For NGC 1068, data at two different pixel scales are shown (corresponding to the solid and dashed brown lines).
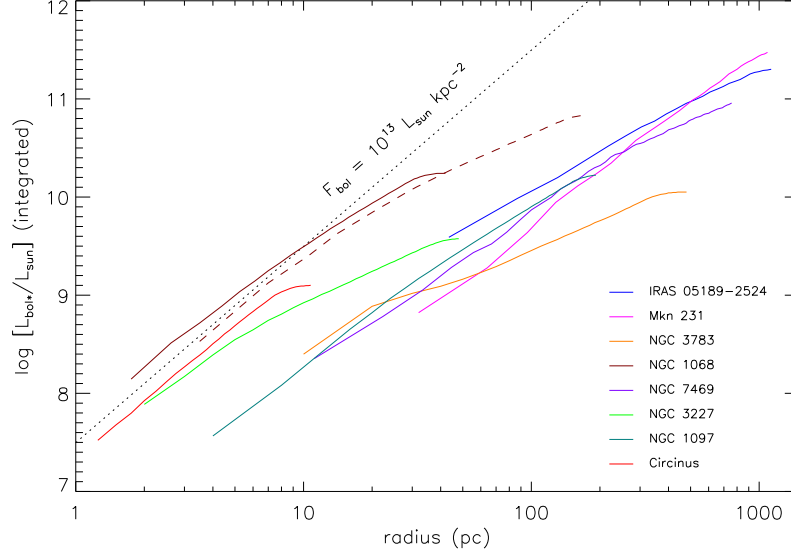
Fig. 9.— Integrated bolometric luminosity of young stars L_{bol*} (see Fig. 8) as a function of radius. For comparison, the dotted line has constant surface brightness. For NGC 1068, data at two different pixel scales are shown (corresponding to the solid and dashed brown lines).
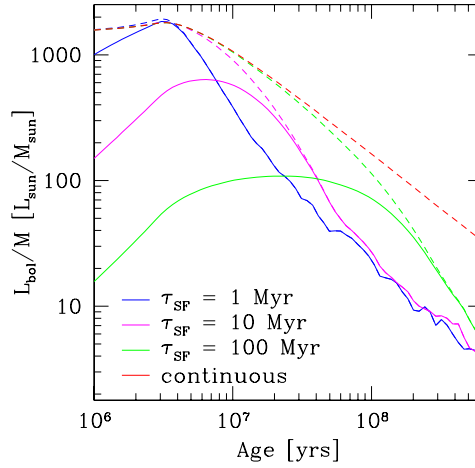
Fig. 10.— Luminosity to mass ratio calculated by STARS as a function of age for different star formation timescales. The dotted lines show how the ratio would vary if gas were fed in to a cluster at the same rate as it was converted into stars. The solid lines assume that the gas is present at the start, but at the end has all been processed in stars. A cluster can only exceed $500\,L_\odot/M_\odot$ for a timescale of $\sim 10\,\mathrm{Myr}$.
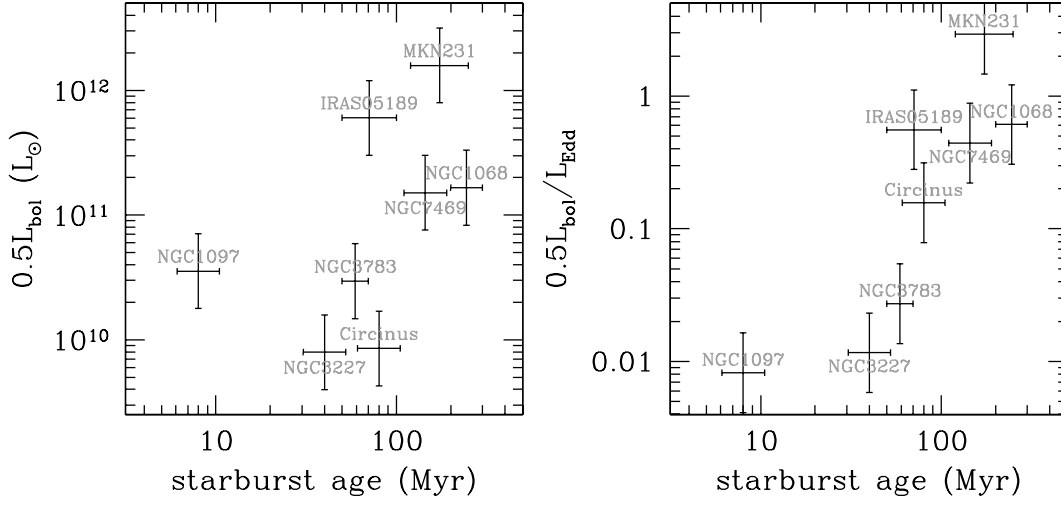
Fig. 11.— Graph showing how the luminosity of an AGN might be related to the age of the most recent episode of nuclear star formation. On the left is shown the luminosity in solar units; on the right, it is with respect to the Eddington luminosity for the black hole. Generally the luminosity of the AGN is not well known and so we have approximated it by $0.5L_{bol}$, and adopted an uncertainty of a factor 2. The starburst age refers to our best estimate of the most recent episode of star formation within the central 10–100 pc, as given in Table 3. See the text for details of the adopted uncertainties.
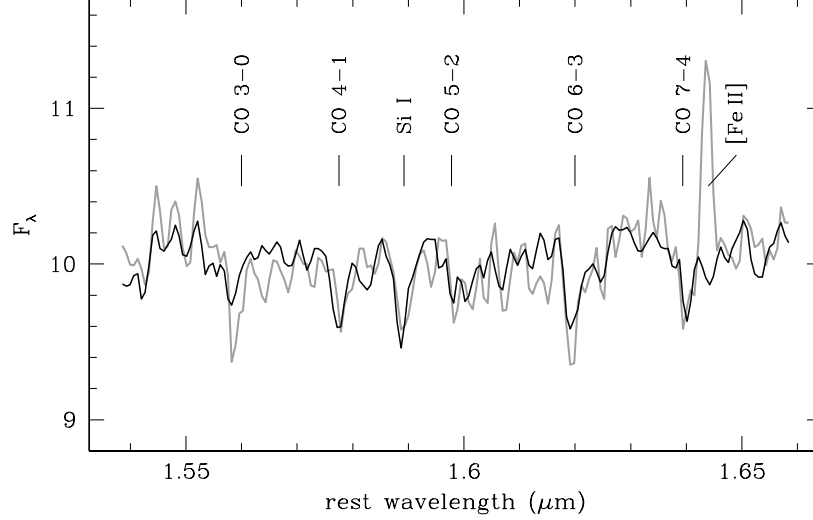
Fig. 12.— Spectrum (in grey) of IRAS 05189-2524, integrated over two 0.22″ wide sections centered ±0.27″ either side of the nucleus, and which have been shifted to match their velocities. Overplotted in black is a fit to the continuum, comprising spectra of various supergiant stars. The main absorption and emission features have been identified.
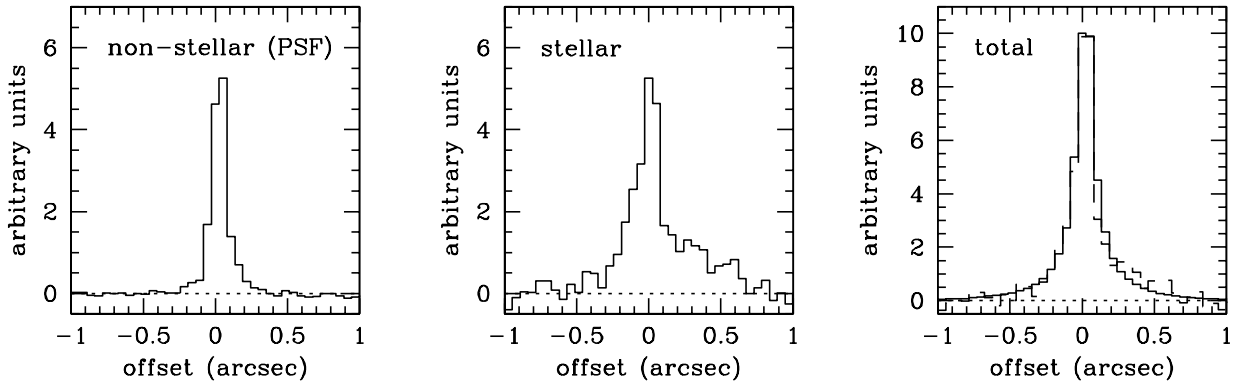
Fig. 13.— Spatial profiles of non-stellar (left), stellar (centre), and total (right) continuum for IRAS 05189-2524 (1″ = 800 pc). The first two have been derived at each point along the spatial extent of the slit from the spectral slope and the stellar absorption features respectively. A comparison of their sum (dashed line in right panel) to the total continuum indicates that the decomposition appears to be reasonable.

stellar continuum   narrow Brγ flux   Brγ velocity   Brγ dispersion
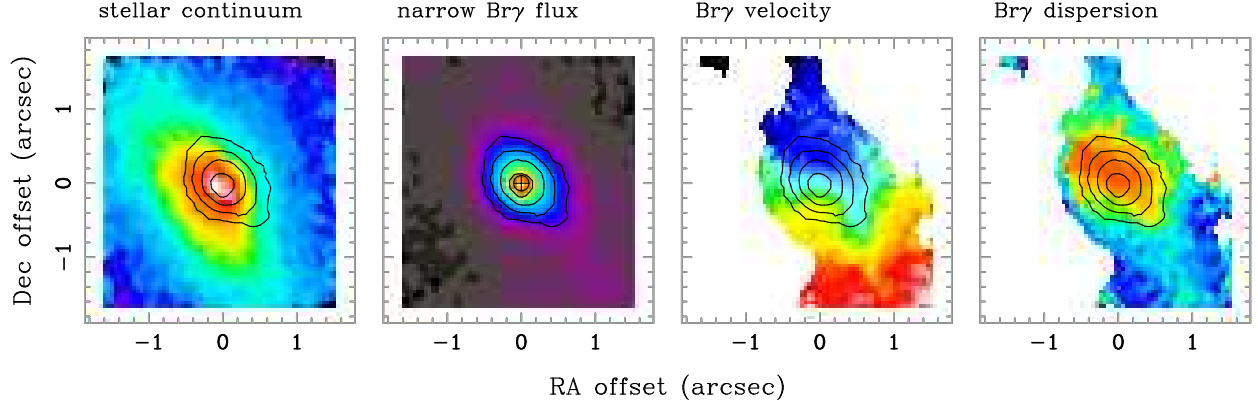
Fig. 14.— Maps of NGC 2992 ($1'' = 160$ pc). From left to right: stellar continuum, narrow Brγ, Brγ velocity (-150 to $+150$ km s^{-1}), and Brγ dispersion (0 to 200 km s^{-1}). For reference, on each panel are superimposed contours of the Brγ flux (8, 16, 32, and 64% of the peak). The symbol plotted on the map of the line flux indicates the centre of the broad Brγ and non-stellar emission. The narrow Brγ emission extends far more to the north west than the stellar continuum. And, particularly on the south western edge, it exhibits a blue shifted velocity and high dispersion. All these are consistent with an interpretation as the apex of an ionisation cone.
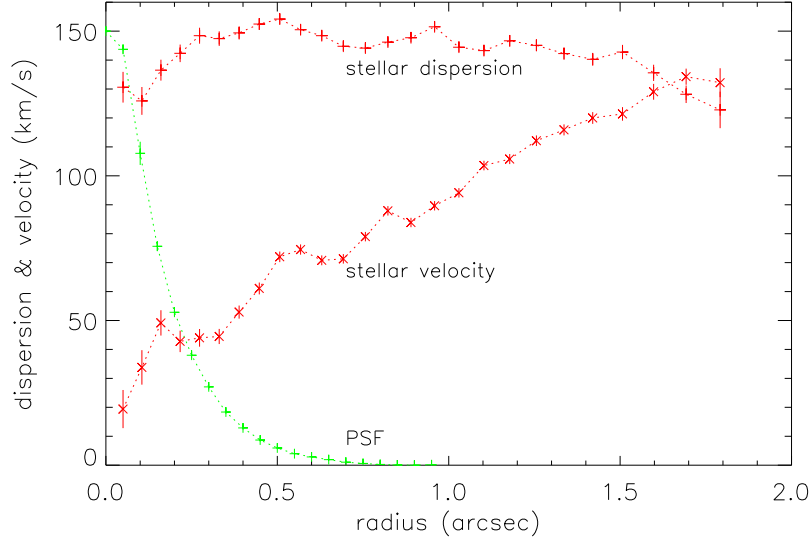
Fig. 15.— Radial profiles of velocity and dispersion for the stars in NGC 2992 ($1'' = 160$ pc). The 2D maps were analysed using the kinemetric technique described by Krajnović et al. (2006) which yielded a position angle of $24°$ and an inclination of $\sim 40°$, not dissimilar to the isophotal values of $30°$ and $50°$ respectively. The rotation curve has been corrected for the inclination.
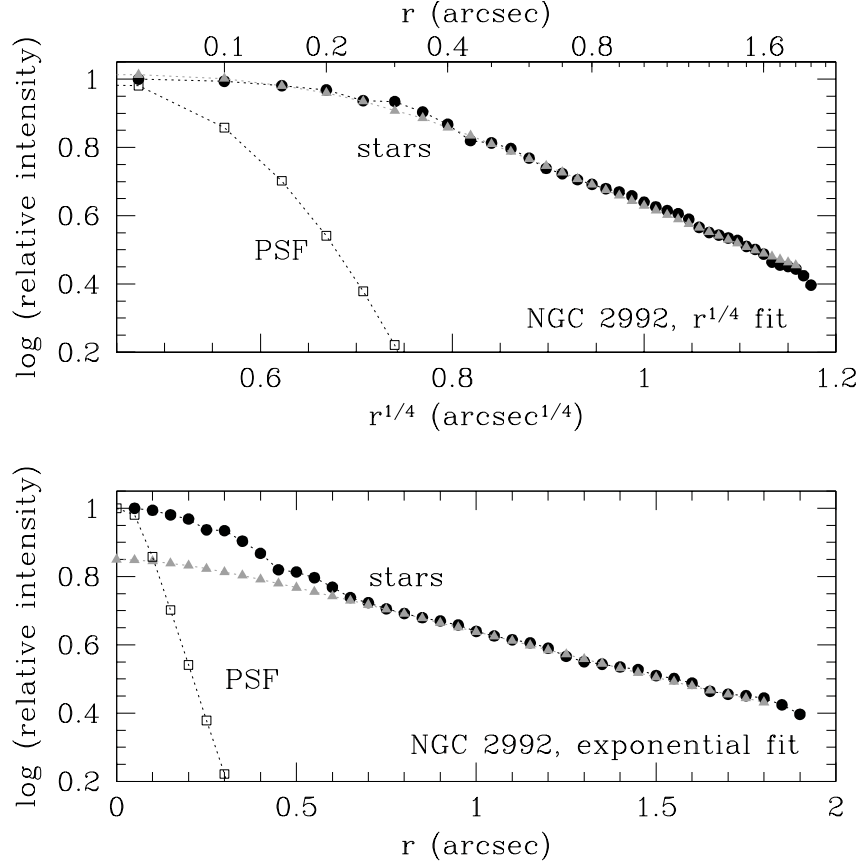
Fig. 16.— Radial profile of the stellar continuum in NGC 2992 ($1'' = 160\,\mathrm{pc}$), derived from isophotal analysis. Solid circles denote the stellar continuum (i.e. already corrected for the non-stellar component). Overplotted with triangles are an $r^{1/4}$ law (top panel) and an exponential profile (bottom panel). The profiles were fitted at radii $r > 0.5''$ and extrapolated inwards, convolved with the PSF which is shown as open squares. Both fits are equally good at $r > 0.5''$, but only the exponential suggests there might be excess continuum at the centre, arising from a distinct stellar population. This is therefore inconclusive.
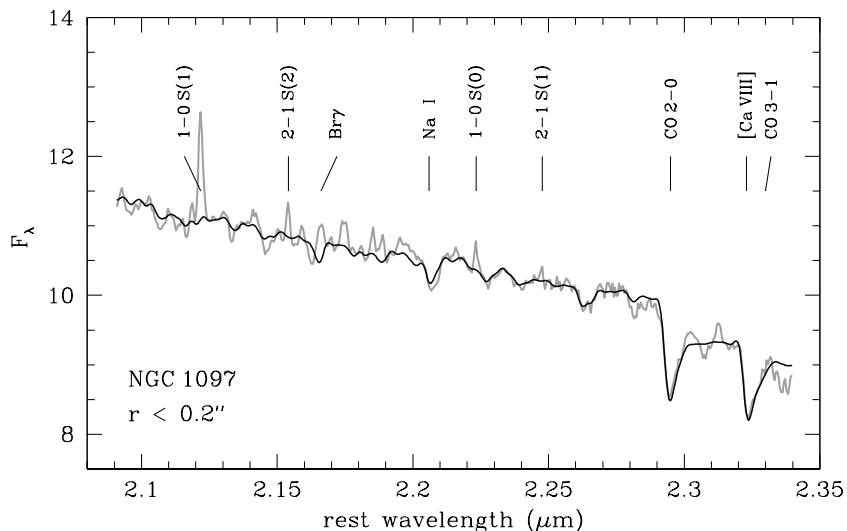
Fig. 17.— Spectrum of NGC 1097 (thick grey line), extracted within an aperture of radius 0.2″ and scaled arbitrarily. Overdrawn (thin black line) is a match to the stellar continuum constructed from template spectra of several late-type supergiant stars and a blackbody function representing the non-stellar component. Notably, Brγ in the nucleus is extremely weak even in the nucleus.
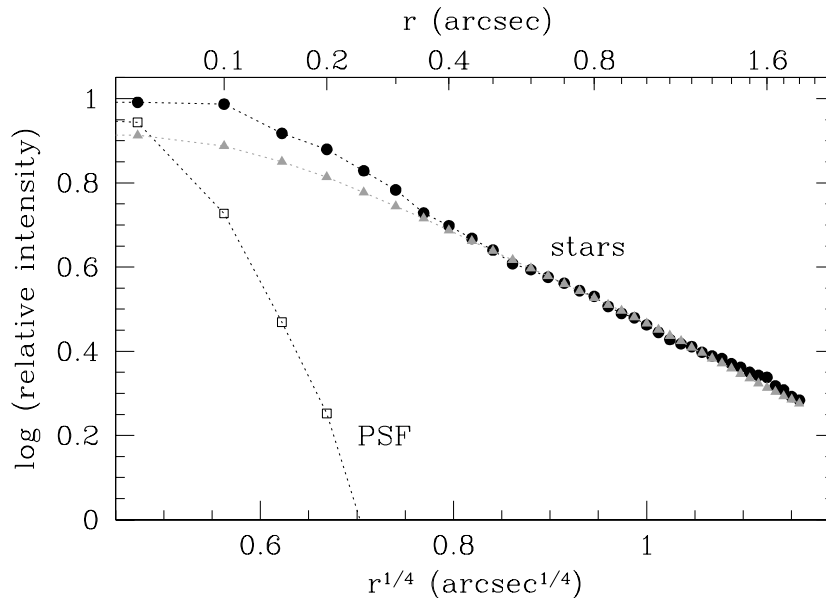
Fig. 18.— Radial profile of the stellar continuum in NGC 1097 (1″ = 80 pc). The solid circles denote the stellar continuum (i.e. already corrected for the non-stellar component). The triangles denote an $r^{1/4}$ profile fitted to radii $r > 0.5″$ and extrapolated inwards. This model has been convolved with the PSF, shown as open squares for comparison. Note that even though an exponential profile might match the data equally well, an $r^{1/4}$ profile provides a stronger constraint on whether there is excess continuum at the centre.
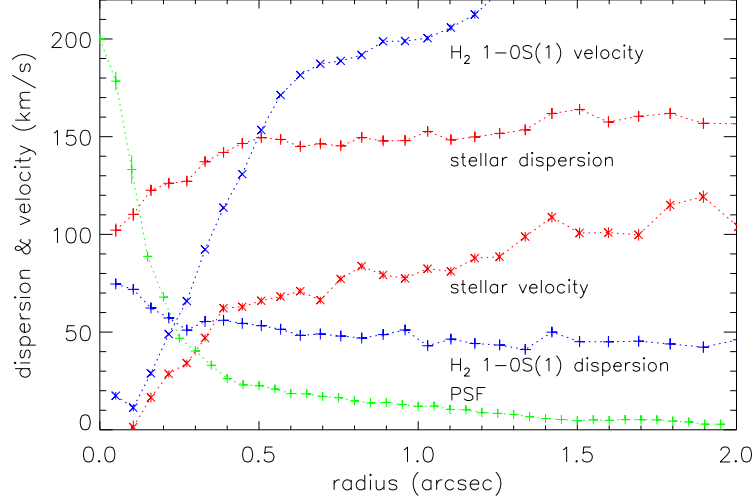
Fig. 19.— Radial profiles of velocity and dispersion for the gas and stars in NGC 1097 ($1'' = 80\,\mathrm{pc}$). The 2D maps were created by convolving template spectra (i.e unresolved line profile for the gas, stellar template for the stars) with a Gaussian and minimising the difference with respect to the galaxy spectrum at each spatial pixel. These were then analysed using the kinemetric technique described by Krajnović et al. (2006) which yielded the same position angle of $-49°$ for the gas and stars, and similar inclinations of $32°$ and $43°$ respectively. The rotation curve has been corrected for the inclination.
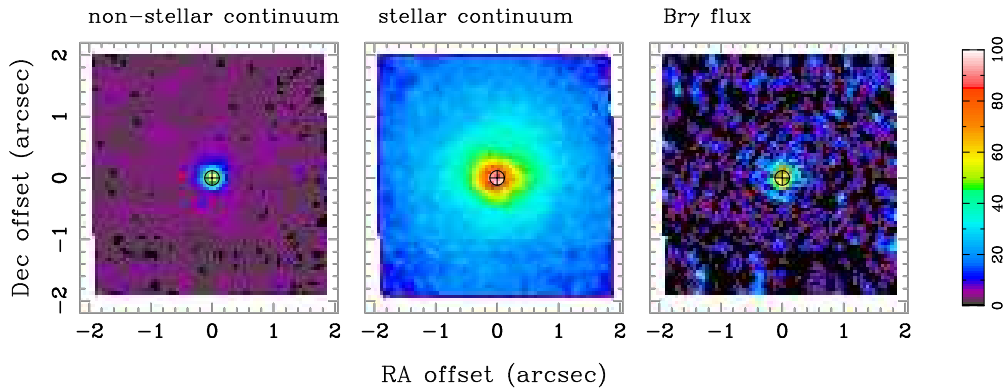
Fig. 20.— Maps of K-band non-stellar continuum (left), stellar continuum (centre), and Brγ line flux (right) for the central few arcsec of NGC 1097 ($1'' = 80\,\mathrm{pc}$). In each case, the centre (as defined by the non-stellar continuum) is marked by a crossed circle. The colour scale is shown on the right, as percentage of the peak in each map.
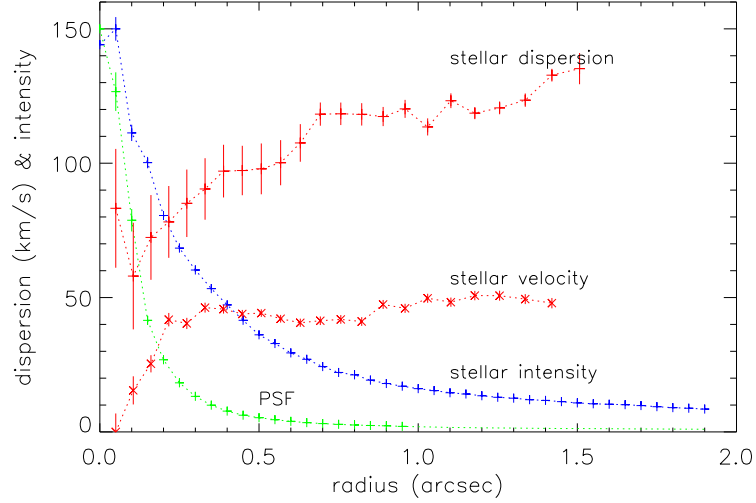
Fig. 21.— Radial profiles of velocity and dispersion for stars in NGC 1068 ($1'' = 70\,\mathrm{pc}$). The 2D maps were then analysed using kinemetry Krajnović et al. (2006), yielding an inclination of $40°$ and a position angle of $85°$. The rotation curve has been corrected for the inclination. Also plotted for comparison are azimuthally averaged radial profiles of the H-band stellar luminosity and the PSF.
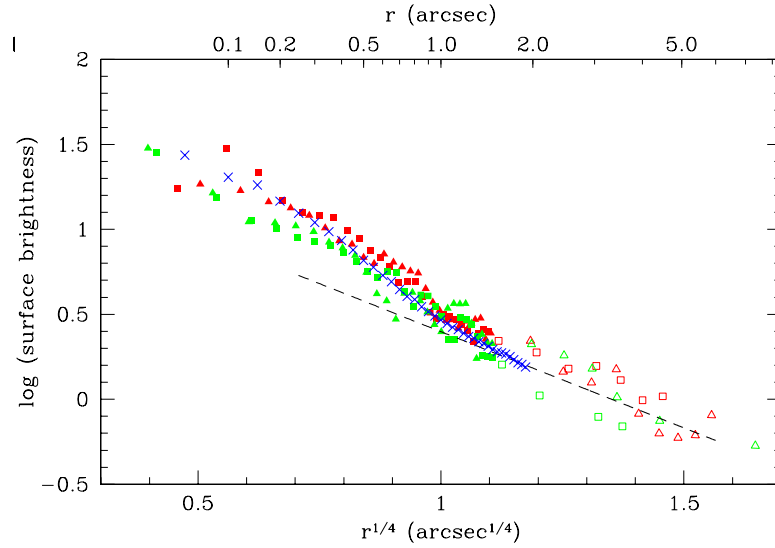

Fig. 22.— Radial profiles of the H-band stellar luminosity in NGC 1068 ($1''= 70\,\mathrm{pc}$) from NACO longslit data at position angle $0°$ and $90°$ (green and red symbols; squares and triangles deonte opposite sides of the nucleus). To trace the profile to larger radius, open symbols are each the mean of 9 points. Superimposed are SINFONI data from Fig. 21 (blue crosses, flux scaled to match). The dashed line denotes an $r^{1/4}$ law with $R_{\mathrm{eff}} = 1.5''$ to match the outer profile. At $r < 1''$, the stellar continuum reveals an excess above the inward extrapolation of this profile.
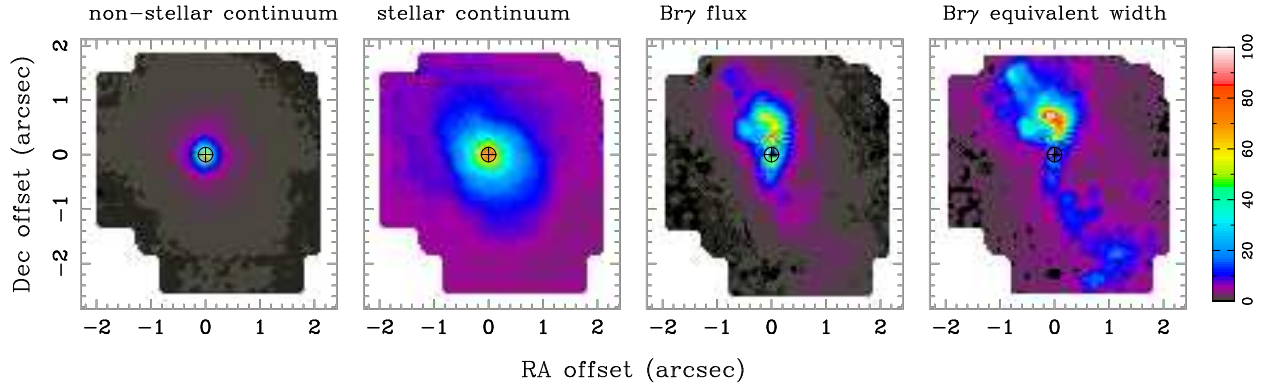
Fig. 23.— Maps of the central few arcsec of NGC 1068 ($1'' = 70\,\mathrm{pc}$): H-band non-stellar continuum (far left) and stellar continuum (centre left); also Brγ line flux (center right) and Brγ equivalent width (far right). In each case, the centre (as defined by the non-stellar continuum) is marked by a crossed circle. The colour scale is shown on the right, as percentage of the peak in each map (and also as $W_{\mathrm{Br}\gamma}$ in Å).
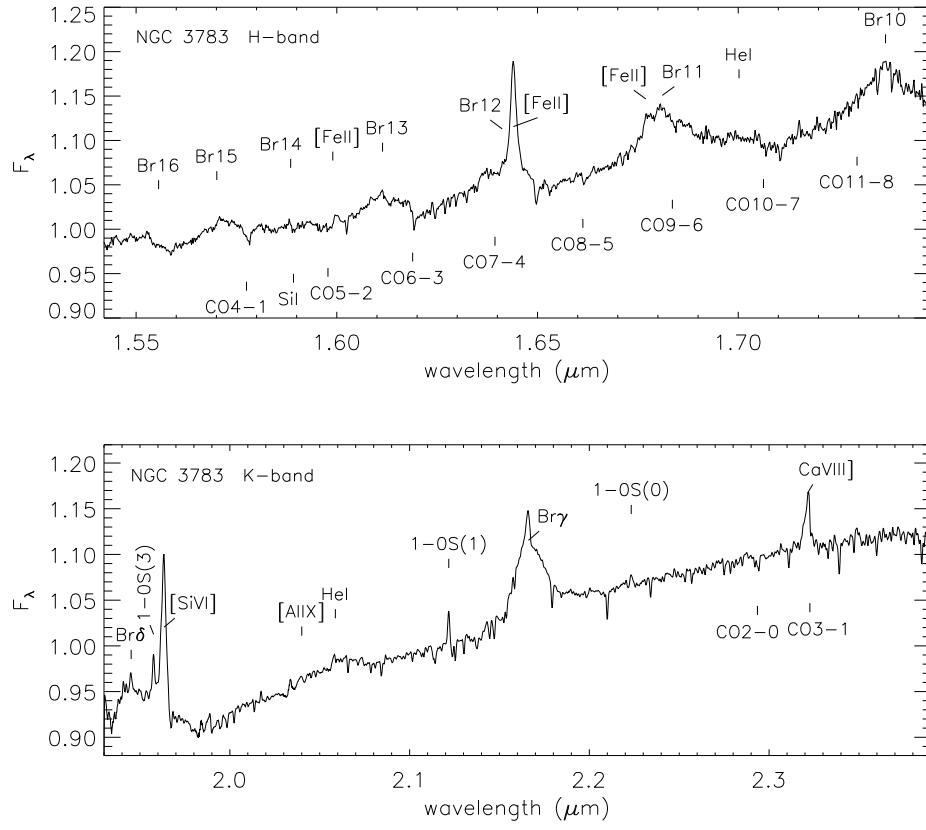
Fig. 24.— H- and K-band spectra of the central 1″ of NGC 3783, with the prominent emission and absorption features labelled. In the H-band it is challenging to measure the stellar absorption due to the very strong brackett emission from the AGN's broad line region. Instead we have used the K-band CO 2-0 bandhead even though the dilution at this wavelength is extreme.
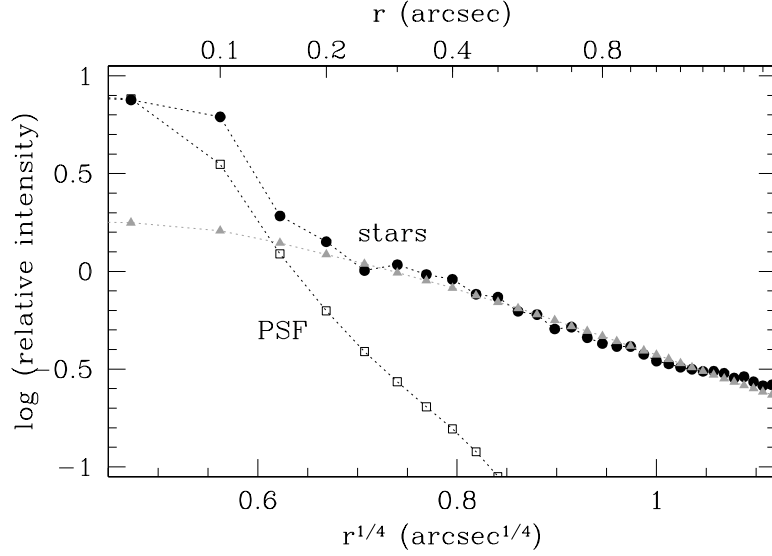
Fig. 25.— Radial profile of the stellar continuum in NGC 3783 ($1'' = 200\,\text{pc}$). The solid circles denote the stellar continuum (i.e. already corrected for the non-stellar component). The triangles denote an $r^{1/4}$ profile fitted to radii $0.2 < r < 1.6''$ and extrapolated inwards. This model has been convolved with the PSF, shown as open squares for comparison. Note that even though an exponential profile might match the data equally well, an $r^{1/4}$ profile provides a stronger constraint on whether there is excess continuum at the centre.
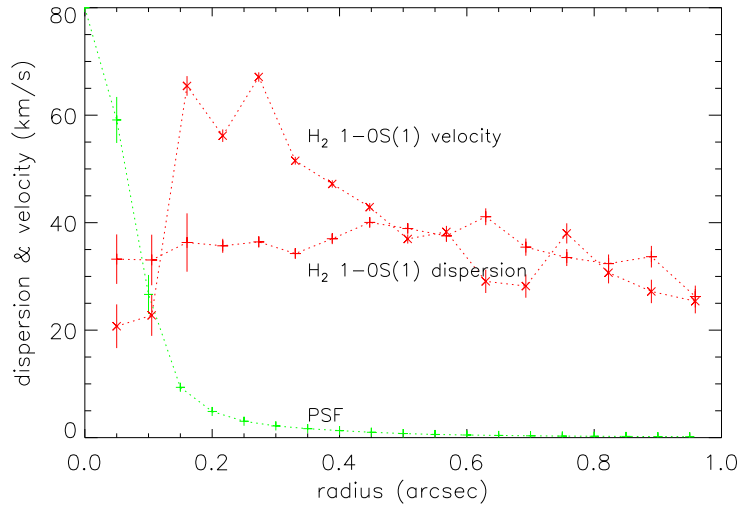

Fig. 26.— Rotation curve derived from the the H_2 1-0 S(1) velocity field in NGC 3783 ($1'' = 200\,\text{pc}$). Also shown is the dispersion as a function of radius. The velocity field was analysed using kinemetry (Krajnović et al. 2006) which yielded a major axis of about $-14°$ and an inclination in the range 35–39°. The drop in velocity at $r < 0.15''$ maybe due to beam smearing across the nucleus.

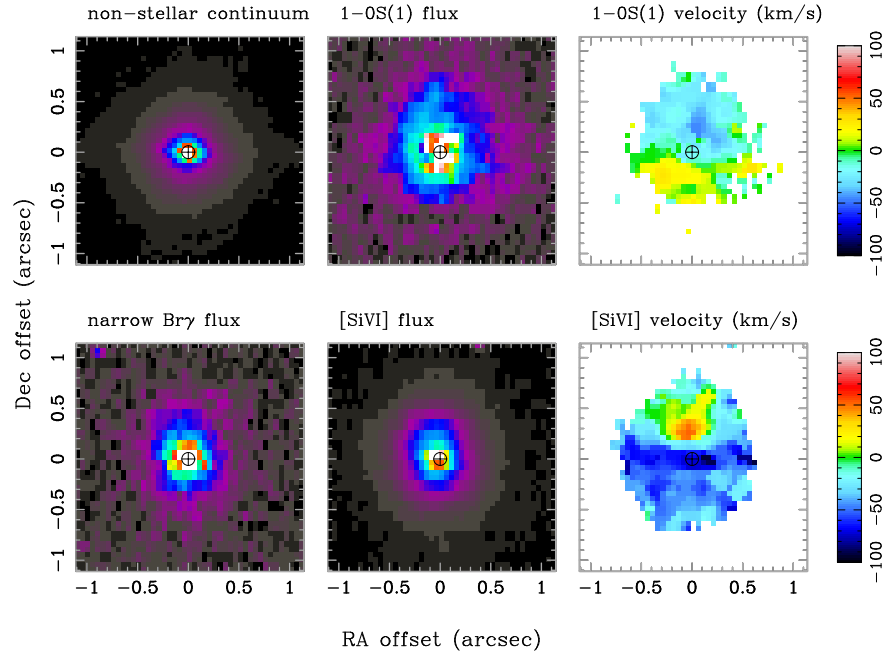Fig. 27.— Images of the central 2″ of NGC 3783 (1″ = 200 pc). Top row from left: non-stellar continuum, H_2 1-0 S(1) line flux, H_2 1-0 S(1) velocity. Bottom row from left: narrow Brγ line flux, [Si VI] line flux, [Si VI] velocity. The Brγ velocity field is similar to that of [Si VI] and shows an outflow of $>50\,\mathrm{km\,s^{-1}}$ to the north. This is in contrast to the 1-0 S(1) velocity field which traces rotation.